Heat transport in two-dimensional materials by directly solving the phonon Boltzmann equation under Callaway's dual relaxation model

Yangyu Guo and Moran Wang*

Key Laboratory for Thermal Science and Power Engineering of Ministry of Education, Department of Engineering Mechanics and CNMM, Tsinghua University, Beijing 100084, China

(Received 5 September 2017; published 30 October 2017)

The single mode relaxation time approximation has been demonstrated to greatly underestimate the lattice thermal conductivity of two-dimensional materials due to the collective effect of phonon normal scattering. Callaway's dual relaxation model represents a good approximation to the otherwise *ab initio* solution of the phonon Boltzmann equation. In this work we develop a discrete-ordinate-method (DOM) scheme for the numerical solution of the phonon Boltzmann equation under Callaway's model. Heat transport in a graphene ribbon with different geometries is modeled by our scheme, which produces results quite consistent with the available molecular dynamics, Monte Carlo simulations, and experimental measurements. Callaway's lattice thermal conductivity model with empirical boundary scattering rates is examined and shown to overestimate or underestimate the direct DOM solution. The length convergence of the lattice thermal conductivity of a rectangular graphene ribbon is explored and found to depend appreciably on the ribbon width, with a semiquantitative correlation provided between the convergence length and the width. Finally, we predict the existence of a phonon Knudsen minimum in a graphene ribbon only at a low system temperature and isotope concentration so that the average normal scattering rate is two orders of magnitude stronger than the intrinsic resistive one. The present work will promote not only the methodology for the solution of the phonon Boltzmann equation but also the theoretical modeling and experimental detection of hydrodynamic phonon transport in two-dimensional materials.

DOI: 10.1103/PhysRevB.96.134312

I. INTRODUCTION

With the rapid developments in nanoscience and nanotechnology in the past several decades, the microscale and nanoscale heat transport have become an important research topic around the world [1–3]. The classical Fourier's law is often no longer valid as the spatial or temporal characteristic dimension has shrunk to be comparable to or even smaller than the mean-free path or relaxation time of heat carriers including molecules, phonons, electrons, photons, and magnons [4,5]. Therefore, extensive study on nanoscale heat transport is motivated by both fundamental understanding of thermal physics at the nanoscale and technical applications in extreme states. One such great technical challenge is the heat dissipation and thermal management of micro- and nanoelectronics [6,7]. People are thus pursing thermal interface materials with high thermal conductivity, among which two-dimensional graphene is a promising choice [8,9] because of its extremely good in-plane thermal transport properties [10,11].

There has been a large number of experimental and theoretical works on heat transport in graphene, as summarized well in two recent review articles [12,13]. The theoretical work mainly consists of two groups: molecular dynamics (MD) simulation and phonon Boltzmann equation modeling. MD simulation is often flawed by the insufficient treatment of quantum effects [14], diverse atomic interaction potential functions [15], and relatively small simulation cells. In contrast, phonon Boltzmann equation modeling is a mesoscopic approach avoiding or relieving the aforementioned three drawbacks [16,17]. The phonon Boltzmann equation approach includes the exact (*ab initio*) solution of the linearized phonon Boltzmann equation with the full scattering term and the relaxation time approximation models. There have been two categories of *ab initio* solution methods: the deterministic one including the iterative approach [18] and variational approach [19], and the stochastic one, i.e., the *ab initio* Monte Carlo scheme [20]. The *ab initio* (or first-principles) method has demonstrated its successful application in predicting the lattice thermal conductivity of graphene ribbons [20–27]. Nevertheless, the implementation of the *ab initio* solution is computationally intensive and often too complicated for engineering utilization; on the other hand, empirical phonon-boundary scattering has been added into the full scattering term in the deterministic methods for heat transport in nanostructures which may introduce a maximum error on the order of 30% in graphene ribbons [20].

The relaxation time approximation models represent a much simpler approach in spite of sacrificing minor accuracy. The commonly used single mode relaxation time (SMRT) approximation [16,17,28,29] has been shown to greatly underestimate the thermal conductivity of graphene ribbons [21,23–25]. This underestimation comes from the collective effect of strong nonresistive phonon normal scattering at all temperature scopes in graphene [24–26]. The SMRT approximation treats equally the normal scattering and resistive scattering (umklapp, isotope, etc.) thus overrating the heat transport resistance. In comparison, Callaway's dual relaxation model [30] has been found as a very good approximation to the *ab initio* results when normal scattering plays a significant role [31] especially in two-dimensional materials (graphene, graphane, etc.) [25]. Callaway's model assumes that the normal scattering and resistive scattering restores the phonon distribution to a displaced Planck distribution and a Planck distribution separately [30]. However, the existing phonon Boltzmann modeling based on Callaway's model for graphene heat transport [32,33] is limited to empirical treatment of

*Corresponding author: mrwang@tsinghua.edu.cn

phonon-boundary scattering based on an additional relaxation term. A direct numerical solution of the phonon Boltzmann equation under Callaway's model is still lacking, which would avoid the empirical boundary treatment in both previous approximate models [32,33] and *ab initio* solutions [21,23,24,27]. The direct numerical solution is also indispensable for modeling heat transport in a rectangular graphene ribbon with finite length and width [34,35], which is generally impossible by the current deterministic *ab initio* method.

One of the main aims in the present work is to develop a numerical scheme for solution of the phonon Boltzmann equation under Callaway's dual relaxation model accounting for the phonon spectral properties. The existing schemes for numerical solution of the phonon Boltzmann equation under the SMRT approximation mainly include the Monte Carlo (MC) scheme [36,37], lattice Boltzmann method (LBM) [38,39], discrete-ordinate-method (DOM) scheme [40,41], finite volume method (FVM) [42,43], and discrete unified gas kinetic scheme (DUGKS) [44,45]. We chose to develop the DOM scheme for the phonon Boltzmann equation under the dual relaxation model for the following reasons: (i) it is challenging to implement adequately phonon normal scattering in the existing MC scheme; (ii) it is difficult to treat effectively the strong nonequilibrium effects and phonon spectral properties in LBM; (iii) the DOM, FVM, and DUGKS are all based on the discrete-ordinate formulation. With the DOM method, we are thus capable of exploring both crucial mathematics and novel physics of heat transport in two-dimensional nanomaterials, as the other aim of this study. The remainder of this article is organized as follows: In Sec. II, the mathematical and numerical methods are introduced including the phonon Boltzmann equation under Callaway's model and the DOM scheme; in Sec. III, we demonstrate a validation of the DOM methodology by modeling heat transport in a graphene ribbon with different kinds of geometries; in Sec. IV, three important applications of our methodology are presented including examining the empirical phonon-boundary scattering expressions and investigating the width-dependent length divergence of lattice thermal conductivity and the phonon Knudsen minimum phenomenon in a graphene ribbon; concluding remarks are made in Sec. V.

II. MATHEMATICAL AND NUMERICAL METHODS

A. Phonon Boltzmann equation under Callaway's model

The phonon Boltzmann equation under Callaway's dual relaxation model is [30,46]

$$\frac{\partial f_\omega}{\partial t} + \mathbf{v}_\mathrm{g}\cdot\nabla f_\omega = \frac{f_\mathrm{R}^\mathrm{eq}(T_\mathrm{loc,R}) - f_\omega}{\tau_\mathrm{R}(\omega,\mathrm{p},T)} + \frac{f_\mathrm{N}^\mathrm{eq}(T_\mathrm{loc,N},\mathbf{u}) - f_\omega}{\tau_\mathrm{N}(\omega,\mathrm{p},T)}, \quad (1)$$

where $f_\omega \equiv f(t,\mathbf{r},\omega,p,\mathbf{\Omega})$ denotes the spectral phonon distribution function, with p the phonon polarization, $\mathbf{v}_\mathrm{g}$ the phonon group velocity, and $\mathbf{\Omega} = \mathbf{v}_\mathrm{g}/v_\mathrm{g}$ the unit vector along the direction of phonon propagation. The local pseudoequilibrium distributions for phonon resistive scattering and normal scattering are the Planck distribution and displaced Planck distribution, respectively:

$$f_\mathrm{R}^\mathrm{eq}(T_\mathrm{loc,R}) = \frac{1}{\exp(\hbar\omega/k_\mathrm{B}T_\mathrm{loc,R})-1}, \quad (2)$$

$$f_\mathrm{N}^\mathrm{eq}(T_\mathrm{loc,N},\mathbf{u}) = \frac{1}{\exp[(\hbar\omega-\hbar\mathbf{k}\cdot\mathbf{u})/k_\mathrm{B}T_\mathrm{loc,N}]-1}, \quad (3)$$

where k_B and $\hbar$ denote separately the Boltzmann constant and reduced Planck constant. In Eq. (3), $\mathbf{k}$ is the wave vector related to the microscopic phonon quasimomentum ($\mathbf{p} = \hbar\mathbf{k}$) whereas $\mathbf{u}$ is a macroscopic phonon drift velocity intimately related to heat flux [3]. The two local pseudotemperatures $T_\mathrm{loc,R}$ and $T_\mathrm{loc,N}$ are introduced to ensure the energy conservation principle during phonon resistive scattering and normal scattering, respectively:

$$\frac{1}{h_0}\sum_\mathrm{p}\int\!\!\int_0^{2\pi}\hbar\omega\frac{f_\mathrm{R}^\mathrm{eq}(T_\mathrm{loc,R})-f_\omega}{\tau_\mathrm{R}(\omega,p,T)}\frac{D(\omega,p)}{2\pi}d\theta d\omega = 0, \quad (4)$$

$$\frac{1}{h_0}\sum_\mathrm{p}\int\!\!\int_0^{2\pi}\hbar\omega\frac{f_\mathrm{N}^\mathrm{eq}(T_\mathrm{loc,N},\mathbf{u})-f_\omega}{\tau_\mathrm{N}(\omega,p,T)}\frac{D(\omega,p)}{2\pi}d\theta d\omega = 0, \quad (5)$$

where h_0 is the thickness of two-dimensional material, of which the wave vector space is two-dimensional characterized by the angular variable $\theta \in [0\ 2\pi]$. $D(\omega,p)$ is the density of phonon states for phonon polarization p. The phonon drift velocity can be computed from the quasimomentum conservation of phonon normal scattering:

$$\frac{1}{h_0}\sum_\mathrm{p}\int\!\!\int_0^{2\pi}\hbar\mathbf{k}\frac{f_\mathrm{N}^\mathrm{eq}(T_\mathrm{loc,N},\mathbf{u})-f_\omega}{\tau_\mathrm{N}(\omega,p,T)}\frac{D(\omega,p)}{2\pi}d\theta d\omega = 0. \quad (6)$$

For simplicity, Eq. (1) is rewritten into a deviational intensity form:

$$\frac{\partial\phi_{\omega,\mathrm{p}}}{\partial t} + \mathbf{v}_\mathrm{g}\cdot\nabla\phi_{\omega,\mathrm{p}} = \frac{\phi_\mathrm{R}^\mathrm{eq}(T_\mathrm{loc,R})-\phi_{\omega,\mathrm{p}}}{\tau_\mathrm{R}(\omega,p,T_0)} + \frac{\phi_\mathrm{N}^\mathrm{eq}(T_\mathrm{loc,N},\mathbf{u})-\phi_{\omega,\mathrm{p}}}{\tau_\mathrm{N}(\omega,p,T_0)}, \quad (7)$$

where the phonon intensity and deviational phonon intensity are defined respectively as $I_{\omega,\mathrm{p}} = v_\mathrm{g}\hbar\omega f_\omega\frac{D(\omega,p)}{2\pi}$ and $\phi_{\omega,\mathrm{p}} = I_{\omega,\mathrm{p}} - I_\mathrm{R}^\mathrm{eq}(T_0)$, with $I_\mathrm{R}^\mathrm{eq}(T_0) = v_\mathrm{g}\hbar\omega f_\mathrm{R}^\mathrm{eq}(T_0)\frac{D(\omega,p)}{2\pi}$. The physical meaning of phonon intensity is the flux of energy per unit time, per unit area, per unit plane angle along the direction of phonon propagation, and per unit frequency interval around ω [47]. It has also been assumed the heat transport takes place within a small temperature difference around a reference temperature T_0 such that the phonon Boltzmann equation (7) is linearized. Under the circumstance of small temperature difference thus small heat flux and phonon drift velocity, the displaced Planck distribution is usually approximated within the first-order Taylor expansion [30]:

$$f_\mathrm{N}^\mathrm{eq}(T_\mathrm{loc,N},\mathbf{u}) \simeq f_\mathrm{R}^\mathrm{eq}(T_\mathrm{loc,N}) + T_\mathrm{loc,N}\frac{\partial f_\mathrm{R}^\mathrm{eq}}{\partial T}\frac{\mathbf{k}\cdot\mathbf{u}}{\omega}. \quad (8)$$

Therefore, the local pseudoequilibrium deviational intensities for phonon resistive scattering and normal scattering are

simplified as

$$\phi_{\mathrm{R}}^{\mathrm{eq}}(T_{\mathrm{loc,R}}) = v_{\mathrm{g}}\frac{C_{\omega,\mathrm{p}}}{2\pi}(T_{\mathrm{loc,R}} - T_0), \tag{9}$$

$$\phi_{\mathrm{N}}^{\mathrm{eq}}(T_{\mathrm{loc,N}},\mathbf{u}) = v_{\mathrm{g}}\frac{C_{\omega,\mathrm{p}}}{2\pi}(T_{\mathrm{loc,N}} - T_0) + v_{\mathrm{g}}\frac{C_{\omega,\mathrm{p}}}{2\pi}T_{\mathrm{loc,N}}\frac{\mathbf{k}\cdot\mathbf{u}}{\omega}, \tag{10}$$

where the spectral heat capacity per unit area of the two-dimensional material is defined as $C_{\omega,\mathrm{p}} = \hbar\omega\frac{\partial f_{\mathrm{R}}^{\mathrm{eq}}}{\partial T}D(\omega,p)$. The local pseudotemperatures $T_{\mathrm{loc,R}}$ and $T_{\mathrm{loc,N}}$ are determined through substituting Eq. (9) and Eq. (10) into the energy conservation conditions Eq. (4) and Eq. (5):

$$T_{\mathrm{loc,R}} - T_0 = \frac{1}{C_{\tau_{\mathrm{R}}}}\sum_{\mathrm{p}}\int\!\!\int_0^{2\pi}\frac{\phi_{\omega,\mathrm{p}}}{\Lambda_{\mathrm{R}}(\omega,p,T_0)}d\theta d\omega, \tag{11}$$

$$T_{\mathrm{loc,N}} - T_0 = \frac{1}{C_{\tau_{\mathrm{N}}}}\sum_{\mathrm{p}}\int\!\!\int_0^{2\pi}\frac{\phi_{\omega,\mathrm{p}}}{\Lambda_{\mathrm{N}}(\omega,p,T_0)}d\theta d\omega, \tag{12}$$

where we have defined $C_{\tau_{\mathrm{R}}} = \sum_{\mathrm{p}}\int\frac{C_{\omega,\mathrm{p}}}{\tau_{\mathrm{R}}(\omega,p,T_0)}d\omega$ and $C_{\tau_{\mathrm{N}}} = \sum_{\mathrm{p}}\int\frac{C_{\omega,\mathrm{p}}}{\tau_{\mathrm{N}}(\omega,p,T_0)}d\omega$ for short notations. The phonon drift velocity is determined by substituting Eq. (10) into the quasimomentum conservation condition Eq. (6):

$$\mathbf{u} = \frac{2}{T_{\mathrm{loc,N}}C^1_{\tau_{\mathrm{N}}}}\sum_{\mathrm{p}}\int\!\!\int_0^{2\pi}\frac{\mathbf{k}}{\omega}\frac{\phi_{\omega,\mathrm{p}}}{\Lambda_{\mathrm{N}}(\omega,p,T_0)}d\theta d\omega, \tag{13}$$

with $C^1_{\tau_{\mathrm{N}}} = \sum_{\mathrm{p}}\int\frac{k^2}{\omega^2}\frac{C_{\omega,\mathrm{p}}}{\tau_{\mathrm{N}}(\omega,p,T_0)}d\omega$ defined for short notation.

To sum up, we obtain the linearized phonon Boltzmann equation (7) under Callaway's model with the local pseudoequilibrium deviational intensities for phonon resistive scattering and normal scattering computed from Eqs. (9)–(13). Once the deviational phonon intensity in Eq. (7) is resolved, the macroscopic variables including temperature and heat flux are then calculated from the following statistical formulas:

$$e^{\mathrm{d}}(t,\mathbf{r}) = \frac{1}{h_0}\sum_{\mathrm{p}}\int\!\!\int_0^{2\pi}\frac{\phi_{\omega,\mathrm{p}}}{v_{\mathrm{g}}}d\theta d\omega = C_V[T(t,\mathbf{r}) - T_0], \tag{14}$$

$$\mathbf{q}(t,\mathbf{r}) = \frac{1}{h_0}\sum_{\mathrm{p}}\int\!\!\int_0^{2\pi}\phi_{\omega,\mathrm{p}}\mathbf{\Omega}d\theta d\omega, \tag{15}$$

where e^{d} represents the deviational energy density and the heat capacity per unit volume for two-dimensional material is defined as $C_V = \frac{1}{h_0}\sum_{\mathrm{p}}\int C_{\omega,\mathrm{p}}d\omega$.

B. Discrete-ordinate-method (DOM) scheme

In this subsection, we develop a discrete-ordinate-method (DOM) scheme for numerical solution of Eq. (7). Since the thermal transport properties are concerned throughout this work, we consider the steady-state heat transport in a two-dimensional material. The generalization of the present numerical scheme to transient heat transport is straightforward and will be conducted in future work for the investigation of second sound in graphene ribbons [25,26,48]. The phonon Boltzmann equation (7) under Callaway's model reduces to

$$\mu\frac{\partial\phi_{\omega,\mathrm{p}}}{\partial x} + \eta\frac{\partial\phi_{\omega,\mathrm{p}}}{\partial y} = \frac{\phi_{\mathrm{R}}^{\mathrm{eq}}(T_{\mathrm{loc,R}}) - \phi_{\omega,\mathrm{p}}}{\Lambda_{\mathrm{R}}(\omega,p,T_0)} + \frac{\phi_{\mathrm{N}}^{\mathrm{eq}}(T_{\mathrm{loc,N}},u_x,u_y) - \phi_{\omega,\mathrm{p}}}{\Lambda_{\mathrm{N}}(\omega,p,T_0)}, \tag{16}$$

where the directional cosine and sine are $\mu = \cos\theta$, $\eta = \sin\theta$. The frequency-dependent phonon mean-free paths for resistive scattering and normal scattering are computed respectively as $\Lambda_{\mathrm{R}}(\omega,p,T_0) = v_{\mathrm{g}}(\omega,p)\tau_{\mathrm{R}}(\omega,p,T_0)$, $\Lambda_{\mathrm{N}}(\omega,p,T_0) = v_{\mathrm{g}}(\omega,p)\tau_{\mathrm{N}}(\omega,p,T_0)$.

1. Spectral and angular discretization

The Gauss-Legendre (G-L) quadrature is adopted for the numerical integration over both the phonon frequency and angular variable in the determination of local pseudoequilibrium deviational intensities Eqs. (9) and (10). Therefore, the spectral and angular spaces are discretized based on the abscissae of the G-L quadrature. To ensure symmetry in the angular space, the integration scope $[0\ 2\pi]$ is divided into two parts, $[0\ \pi]$ and $[\pi\ 2\pi]$; for each a G-L quadrature with an equal number of abscissae $N_\theta/2$ is applied. For frequency integration, a G-L quadrature is applied with the number of abscissae N_p for the phonon polarization p. The discrete local pseudoequilibrium deviational intensities for phonon resistive scattering and normal scattering are thus obtained respectively:

$$\left(\phi_{\mathrm{pR}}^{\mathrm{eq}}\right)_n = (v_{\mathrm{gp}})_n\frac{(C_{\mathrm{p}})_n}{4C_{\tau_{\mathrm{R}}}}\sum_{\mathrm{p}'}\left[\frac{1}{2}\omega_{\mathrm{p}',\mathrm{m}}\sum_{k'=1}^{\mathrm{N}_\theta}\sum_{n'=1}^{\mathrm{N_p}}\frac{(\phi_{\mathrm{p}'})^{k'}_{n'}}{(\Lambda_{\mathrm{p}'\mathrm{R}})_{n'}}\omega_{k'}\omega_{n'}\right], \tag{17}$$

$$\begin{aligned}\left(\phi_{\mathrm{pN}}^{\mathrm{eq}}\right)^k_n = {}& (v_{\mathrm{gp}})_n\frac{(C_{\mathrm{p}})_n}{4C_{\tau_{\mathrm{N}}}}\sum_{\mathrm{p}'}\left[\frac{1}{2}\omega_{\mathrm{p}',\mathrm{m}}\sum_{k'=1}^{\mathrm{N}_\theta}\sum_{n'=1}^{\mathrm{N_p}}\frac{(\phi_{\mathrm{p}'})^{k'}_{n'}}{(\Lambda_{\mathrm{p}'\mathrm{N}})_{n'}}\omega_{k'}\omega_{n'}\right]\\ &+ (v_{\mathrm{gp}})_n\frac{(C_{\mathrm{p}})_n}{2C^1_{\tau_{\mathrm{N}}}}\frac{\mu_k(k_{\mathrm{p}})_n}{(\omega_{\mathrm{p}})_n}\sum_{\mathrm{p}'}\left[\frac{1}{2}\omega_{\mathrm{p}',\mathrm{m}}\sum_{k'=1}^{\mathrm{N}_\theta}\sum_{n'=1}^{\mathrm{N_p}}\frac{\mu_{k'}(k_{\mathrm{p}'})_{n'}}{(\omega_{\mathrm{p}'})_{n'}}\frac{(\phi_{\mathrm{p}'})^{k'}_{n'}}{(\Lambda_{\mathrm{p}'\mathrm{N}})_{n'}}\omega_{k'}\omega_{n'}\right]\\ &+ (v_{\mathrm{gp}})_n\frac{(C_{\mathrm{p}})_n}{2C^1_{\tau_{\mathrm{N}}}}\frac{\eta_k(k_{\mathrm{p}})_n}{(\omega_{\mathrm{p}})_n}\sum_{\mathrm{p}'}\left[\frac{1}{2}\omega_{\mathrm{p}',\mathrm{m}}\sum_{k'=1}^{\mathrm{N}_\theta}\sum_{n'=1}^{\mathrm{N_p}}\frac{\eta_{k'}(k_{\mathrm{p}'})_{n'}}{(\omega_{\mathrm{p}'})_{n'}}\frac{(\phi_{\mathrm{p}'})^{k'}_{n'}}{(\Lambda_{\mathrm{p}'\mathrm{N}})_{n'}}\omega_{k'}\omega_{n'}\right]\end{aligned} \tag{18}$$

where $n = 1,2,\ldots,N_p$ are the discrete spectral nodes for phonon polarization p and $k = 1,2,\ldots,N_\theta$ are the discrete angular nodes for the full space $[0\ 2\pi]$, with ω_n, ω_k being the corresponding weight coefficients. The upper limit of spectral integration scope $[0,\omega_{\mathrm{p,m}}]$ represents the maximum phonon frequency of phonon polarization p. The discrete form of Eq. (16) in the spectral and angular space is thus derived:

$$\mu_k\frac{\partial(\phi_\mathrm{p})_n^k}{\partial x}+\eta_k\frac{\partial(\phi_\mathrm{p})_n^k}{\partial y}=\frac{\left(\phi_\mathrm{pR}^\mathrm{eq}\right)_n-(\phi_\mathrm{p})_n^k}{(\Lambda_\mathrm{pR})_n}+\frac{\left(\phi_\mathrm{pN}^\mathrm{eq}\right)_n^k-(\phi_\mathrm{p})_n^k}{(\Lambda_\mathrm{pN})_n}. \tag{19}$$

2. Spatial discretization

To ensure numerical stability and accuracy, the step scheme [40,49] is adopted for spatial discretization. For the first quadrant of angular space wherein $\mu>0$, $\eta>0$, the forward difference scheme is used for both x-direction and y-direction spatial derivatives in Eq. (19):

$$\mu_k\frac{(\phi_\mathrm{p})_{n,i,j}^k-(\phi_\mathrm{p})_{n,i-1,j}^k}{\Delta x}+\eta_k\frac{(\phi_\mathrm{p})_{n,i,j}^k-(\phi_\mathrm{p})_{n,i,j-1}^k}{\Delta y}=\frac{\left(\phi_\mathrm{pR}^\mathrm{eq}\right)_{n,i,j}-(\phi_\mathrm{p})_{n,i,j}^k}{(\Lambda_\mathrm{pR})_n}+\frac{\left(\phi_\mathrm{pN}^\mathrm{eq}\right)_{n,i,j}^k-(\phi_\mathrm{p})_{n,i,j}^k}{(\Lambda_\mathrm{pN})_n}. \tag{20}$$

For the second quadrant of angular space wherein $\mu<0$, $\eta>0$, the backward and forward differences are used respectively for x-direction and y-direction spatial derivatives in Eq. (19):

$$\mu_k\frac{(\phi_\mathrm{p})_{n,i+1,j}^k-(\phi_\mathrm{p})_{n,i,j}^k}{\Delta x}+\eta_k\frac{(\phi_\mathrm{p})_{n,i,j}^k-(\phi_\mathrm{p})_{n,i,j-1}^k}{\Delta y}=\frac{\left(\phi_\mathrm{pR}^\mathrm{eq}\right)_{n,i,j}-(\phi_\mathrm{p})_{n,i,j}^k}{(\Lambda_\mathrm{pR})_n}+\frac{\left(\phi_\mathrm{pN}^\mathrm{eq}\right)_{n,i,j}^k-(\phi_\mathrm{p})_{n,i,j}^k}{(\Lambda_\mathrm{pN})_n}. \tag{21}$$

For the third quadrant of angular space wherein $\mu<0$, $\eta<0$, the backward difference is used for both x-direction and y-direction spatial derivatives in Eq. (19):

$$\mu_k\frac{(\phi_\mathrm{p})_{n,i+1,j}^k-(\phi_\mathrm{p})_{n,i,j}^k}{\Delta x}+\eta_k\frac{(\phi_\mathrm{p})_{n,i,j+1}^k-(\phi_\mathrm{p})_{n,i,j}^k}{\Delta y}=\frac{\left(\phi_\mathrm{pR}^\mathrm{eq}\right)_{n,i,j}-(\phi_\mathrm{p})_{n,i,j}^k}{(\Lambda_\mathrm{pR})_n}+\frac{\left(\phi_\mathrm{pN}^\mathrm{eq}\right)_{n,i,j}^k-(\phi_\mathrm{p})_{n,i,j}^k}{(\Lambda_\mathrm{pN})_n}. \tag{22}$$

For the fourth quadrant of angular space wherein $\mu>0$, $\eta<0$, the forward and backward differences are used respectively for x-direction and y-direction spatial derivatives in Eq. (19):

$$\mu_k\frac{(\phi_\mathrm{p})_{n,i,j}^k-(\phi_\mathrm{p})_{n,i-1,j}^k}{\Delta x}+\eta_k\frac{(\phi_\mathrm{p})_{n,i,j+1}^k-(\phi_\mathrm{p})_{n,i,j}^k}{\Delta y}=\frac{\left(\phi_\mathrm{pR}^\mathrm{eq}\right)_{n,i,j}-(\phi_\mathrm{p})_{n,i,j}^k}{(\Lambda_\mathrm{pR})_n}+\frac{\left(\phi_\mathrm{pN}^\mathrm{eq}\right)_{n,i,j}^k-(\phi_\mathrm{p})_{n,i,j}^k}{(\Lambda_\mathrm{pN})_n}. \tag{23}$$

In Eqs. (20)–(23), $i = 1,2,\ldots,N_x$ and $j = 1,2,\ldots,N_y$ represent the spatial nodes in the x direction and y direction, respectively.

The discrete deviational phonon intensities are thus derived from Eqs. (20)–(23) for the first to fourth quadrants separately:

$$(\phi_\mathrm{p})_{n,i,j}^k=\frac{(m_\mathrm{p})_n^k(\phi_\mathrm{p})_{n,i-1,j}^k+(n_\mathrm{p})_n^k(\phi_\mathrm{p})_{n,i,j-1}^k+\frac{(\Lambda_\mathrm{pC})_n}{(\Lambda_\mathrm{pR})_n}\left(\phi_\mathrm{pR}^\mathrm{eq}\right)_{n,i,j}+\frac{(\Lambda_\mathrm{pC})_n}{(\Lambda_\mathrm{pN})_n}\left(\phi_\mathrm{pN}^\mathrm{eq}\right)_{n,i,j}^k}{(m_\mathrm{p})_n^k+(n_\mathrm{p})_n^k+1}, \tag{24}$$

$$(\phi_\mathrm{p})_{n,i,j}^k=\frac{-(m_\mathrm{p})_n^k(\phi_\mathrm{p})_{n,i+1,j}^k+(n_\mathrm{p})_n^k(\phi_\mathrm{p})_{n,i,j-1}^k+\frac{(\Lambda_\mathrm{pC})_n}{(\Lambda_\mathrm{pR})_n}\left(\phi_\mathrm{pR}^\mathrm{eq}\right)_{n,i,j}+\frac{(\Lambda_\mathrm{pC})_n}{(\Lambda_\mathrm{pN})_n}\left(\phi_\mathrm{pN}^\mathrm{eq}\right)_{n,i,j}^k}{-(m_\mathrm{p})_n^k+(n_\mathrm{p})_n^k+1}, \tag{25}$$

$$(\phi_\mathrm{p})_{n,i,j}^k=\frac{-(m_\mathrm{p})_n^k(\phi_\mathrm{p})_{n,i+1,j}^k-(n_\mathrm{p})_n^k(\phi_\mathrm{p})_{n,i,j+1}^k+\frac{(\Lambda_\mathrm{pC})_n}{(\Lambda_\mathrm{pR})_n}\left(\phi_\mathrm{pR}^\mathrm{eq}\right)_{n,i,j}+\frac{(\Lambda_\mathrm{pC})_n}{(\Lambda_\mathrm{pN})_n}\left(\phi_\mathrm{pN}^\mathrm{eq}\right)_{n,i,j}^k}{-(m_\mathrm{p})_n^k-(n_\mathrm{p})_n^k+1}, \tag{26}$$

$$(\phi_\mathrm{p})_{n,i,j}^k=\frac{(m_\mathrm{p})_n^k(\phi_\mathrm{p})_{n,i-1,j}^k-(n_\mathrm{p})_n^k(\phi_\mathrm{p})_{n,i,j+1}^k+\frac{(\Lambda_\mathrm{pC})_n}{(\Lambda_\mathrm{pR})_n}\left(\phi_\mathrm{pR}^\mathrm{eq}\right)_{n,i,j}+\frac{(\Lambda_\mathrm{pC})_n}{(\Lambda_\mathrm{pN})_n}\left(\phi_\mathrm{pN}^\mathrm{eq}\right)_{n,i,j}^k}{(m_\mathrm{p})_n^k-(n_\mathrm{p})_n^k+1}, \tag{27}$$

where $(m_\mathrm{p})_n^k=\frac{\mu_k(\Lambda_\mathrm{pC})_n}{\Delta x}$, $(n_\mathrm{p})_n^k=\frac{\eta_k(\Lambda_\mathrm{pC})_n}{\Delta y}$ are introduced for short notations, with the combinational phonon mean-free path defined as $\frac{1}{\Lambda_\mathrm{pC}}=\frac{1}{\Lambda_\mathrm{pR}}+\frac{1}{\Lambda_\mathrm{pN}}$.

3. Macroscopic variables calculation

Once the discrete deviational phonon intensities are resolved, the temperature distribution and heat flux distribution can be calculated through a discretization of Eqs. (14) and (15), respectively:

$$e^\mathrm{d}(x,y)=\frac{\pi}{2h_0}\sum_\mathrm{p}\frac{1}{2}\omega_{\mathrm{m,p}}\sum_{k=1}^{\mathrm{N}_\theta}\sum_{n=1}^{\mathrm{N}_\mathrm{p}}\frac{(\phi_\mathrm{p})_{n,i,j}^k}{(v_\mathrm{gp})_n}\omega_k\omega_n=C_V[T(x,y)-T_0], \tag{28}$$

$$q_x(x,y)=\frac{\pi}{2h_0}\sum_\mathrm{p}\frac{1}{2}\omega_{\mathrm{m,p}}\sum_{k=1}^{\mathrm{N}_\theta}\sum_{n=1}^{\mathrm{N}_\mathrm{p}}\mu_k(\phi_\mathrm{p})_{n,i,j}^k\omega_k\omega_n, \tag{29}$$

$$q_y(x,y) = \frac{\pi}{2h_0}\sum_{\mathrm{p}}\frac{1}{2}\omega_{\mathrm{m,p}}\sum_{k=1}^{\mathrm{N}_\theta}\sum_{n=1}^{\mathrm{N_p}}\eta_k(\phi_{\mathrm{p}})^k_{n,i,j}\omega_k\omega_n. \quad (30)$$

C. Boundary treatments

1. Isothermal boundary condition

The isotropic Planck equilibrium distribution is adopted for the distribution function of phonons incident to the medium from the isothermal surface. Under the linearized assumptions made in Sec. II A, the boundary conditions for the left-hand hot source at T_{h} and right-hand cold source at T_{c} of a graphene ribbon with a length L are respectively

$$\phi_{\omega,\mathrm{p}}(x=0,\mu>0) = v_{\mathrm{g}}\frac{C_{\omega,\mathrm{p}}}{2\pi}(T_{\mathrm{h}}-T_0), \quad (31)$$

$$\phi_{\omega,\mathrm{p}}(x=L,\mu<0) = v_{\mathrm{g}}\frac{C_{\omega,\mathrm{p}}}{2\pi}(T_{\mathrm{c}}-T_0). \quad (32)$$

2. Adiabatic boundary condition

Two kinds of numerical treatments are available for the adiabatic boundary: the specular scheme and diffuse scheme. Due to the edge roughness of two-dimensional materials, the diffuse scheme is often a good approximation for the adiabatic boundary treatment [20]. The diffuse scheme assumes that the direction of phonons leaving from the boundary is independent of that of the incident phonons. We adopt the nonthermalizing diffuse scheme for the bottom and top adiabatic boundaries of a graphene ribbon with a width W to ensure accurate energy conservation:

$$\phi_{\omega,\mathrm{p}}(x,y=0,\eta>0) = -\frac{\int_{\pi}^{2\pi}\phi_{\omega,\mathrm{p}}(x,y=0)\eta d\theta}{\int_0^{\pi}\eta d\theta}, \quad (33)$$

$$\phi_{\omega,\mathrm{p}}(x,y=W,\eta<0) = -\frac{\int_0^{\pi}\phi_{\omega,\mathrm{p}}(x,y=W)\eta d\theta}{\int_{\pi}^{2\pi}\eta d\theta}. \quad (34)$$

It is crucial to calculate the integration in the denominators in Eqs. (33) and (34) through the same G-L quadrature as the numerators therein; otherwise the numerical results will be distorted due to the minor discretization error.

3. Periodic heat flux boundary condition

The periodic heat flux boundary condition is important in both DOM [50] and Monte Carlo (MC) [51] solutions of the phonon Boltzmann equation for modeling heat transport in periodic nanostructures based on only one unit element. Its main idea is to implement a constant heat flux along the temperature gradient direction through the same distortion of the phonon distribution function from equilibrium at two ends of the simulation domain. This scheme is used for heat transport in an infinitely long sample to avoid a large number of spatial grids along the length direction:

$$\phi_{\omega,\mathrm{p}}(x=0,\mu>0) = v_{\mathrm{g}}\frac{C_{\omega,\mathrm{p}}}{2\pi}(T_{\mathrm{h}}-T_{\mathrm{c}}) + \phi_{\omega,\mathrm{p}}(x=L,\mu>0), \quad (35)$$

$$\phi_{\omega,\mathrm{p}}(x=L,\mu<0) = v_{\mathrm{g}}\frac{C_{\omega,\mathrm{p}}}{2\pi}(T_{\mathrm{c}}-T_{\mathrm{h}}) + \phi_{\omega,\mathrm{p}}(x=0,\mu<0), \quad (36)$$

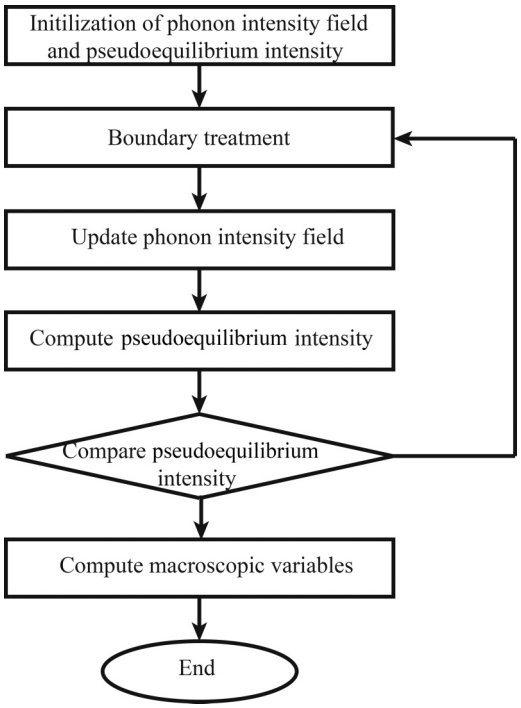

FIG. 1. Schematic of the algorithm procedure for the discrete-ordinate-method (DOM) solution of the phonon Boltzmann equation under Callaway's model.

where L is the length of the simulation domain with T_{h} and T_{c} being the specified temperature of its left-hand and right-hand ends, respectively.

D. Algorithm procedure

The discrete-ordinate-method (DOM) solution of the phonon Boltzmann equation under Callaway's model is implemented through an iteration process. Within each iteration step, the solution is put forward from the boundary nodes for each quadrant of angular space based on Eqs. (24)–(27). For instance, the solution starts from the bottom-left boundaries for discrete deviational phonon intensities the direction of which lies within the first quadrant ($\theta \in [0\ \frac{\pi}{2}]$). The discrete deviational phonon intensity field is updated for each discrete spectral node and angular node. Then the local pseudoequilibrium deviational phonon intensities for resistive scattering and normal scattering are computed based on Eq. (17) and Eq. (18), respectively. The iteration process is repeated until the relative difference of local pseudoequilibrium deviational intensities (for both normal scattering and resistive scattering) between two successive iteration steps is smaller than 1×10^{-10}. After the convergence of the iteration process, the macroscopic variables are calculated based on Eqs. (28)–(30) before the end of the whole solution. The algorithm procedure of the numerical solution is summarized in Fig. 1.

III. METHODOLOGY VALIDATIONS

In this section, the discrete-ordinate-method (DOM) scheme developed in Sec. II will be validated by several classical cases in the typical two-dimensional material graphene:

heat transport in an infinitely wide graphene ribbon, heat transport in an infinitely long graphene ribbon, and heat transport in a rectangular graphene ribbon. Since an analytical solution of the phonon Boltzmann equation under Callaway's dual relaxation model for nanoscale heat transport is impossible, we compare the present DOM solution to available benchmark results from MD simulations, the *ab initio* MC solution of the phonon Boltzmann equation, and experimental measurements.

For simplicity without losing accuracy, the phonon dispersion relation along the Γ-M direction with high symmetry is adopted to represent the dispersion of graphene in the first Brillouin zone. There are six phonon polarizations including three acoustic ones and three optical ones, as each unit cell of the graphene lattice has two carbon atoms. The optical phonon polarizations are not taken into account due to their negligible contribution to heat transport because of small group velocities. For both the in-plane longitudinal acoustic (LA) and transverse acoustic (TA) phonon polarizations, the linear expression is a good approximation for the dispersion relation [11]: $\omega = v_g k$, with the group speeds $v_{g,LA} = 2.13 \times 10^4$(m/s) and $v_{g,\,TA} = 1.36 \times 10^4$(m/s). For the out-of-plane flexural acoustic (ZA) phonon polarization, the dispersion relation is approximately quadratic [11]: $\omega = \alpha k^2$, with $\alpha = 6.2 \times 10^{-7}$ (m^2/s). The edge of the first Brillouin zone is located at maximum wave number $k_m = 1.5 \times 10^{10}$ (m^{-1}).

The empirical power-law relaxation time expressions for phonon scattering [52] are incorporated into the present numerical model. In principle, the *ab initio* phonon scattering rate in the entire first Brillouin zone should be taken into account for an accurate prediction of lattice thermal conductivity. Yet the present study can provide still important quasiquantitative results and qualitative indications once the empirical expressions of relaxation time are parametrized for an infinite graphene ribbon (bulk limit). Two categories of intrinsic phonon scattering are considered: (i) resistive scattering including three-phonon umklapp scattering and phonon-isotope scattering, and (ii) three-phonon normal scattering. The phonon relaxation time for three-phonon umklapp scattering is [17,52]

$$\frac{1}{\tau_U(\omega,p,T)} = B_U \omega^2 T \exp(-\Theta_p/3T), \tag{37}$$

where $B_U = \frac{\hbar\gamma_p^2}{\overline{M}\Theta_p v_{g,p}^2}$. The Grüneisen parameters and Debye temperatures for different phonon polarizations are separately $\gamma_{LA} = 2$, $\gamma_{TA} = 2/3$, and $\gamma_{ZA} = -1.5$, and $\Theta_{LA} = 1826.39$ K, $\Theta_{TA} = 1126.18$ K, and $\Theta_{ZA} = 623.62$ K [17,28]. The average mass per carbon atom is computed as $\overline{M} = \sum_i f_i M_i = 12 + c$, with M_i and f_i the atomic mass and mass fraction of each isotope, and c being the abundancy of ^{13}C. The natural abundancy of ^{13}C in graphene is $c = 1.1\%$. The phonon relaxation time for three-phonon normal scattering is [32,33,52]

$$\frac{1}{\tau_N(\omega,p,T)} = B_N \omega^{a_N} T^{b_N}, \tag{38}$$

where $B_N = (\frac{k_B}{\hbar})^{b_N} \frac{\hbar\gamma_p^2 V_0^{(a_N+b_N-2)/3}}{\overline{M} v_{g,p}^{a_N+b_N}}$ with $V_0 = 8.769634 \times 10^{-30}$ m^3 the average volume per carbon atom in graphene. The coefficient pair $a_N = 1$, $b_N = 3$ is chosen as suggested in recent work [33]. For the phonon-isotope scattering, we use the following relaxation time expression [23]:

$$\frac{1}{\tau_I(\omega,p)} = \begin{cases} \frac{\pi}{2}\Gamma S_0 \omega^2 D(\omega,p), & \text{for } p = \text{ZA}, \\ \frac{\pi}{4}\Gamma S_0 \omega^2 D(\omega,p), & \text{for } p = \text{LA,TA}, \end{cases} \tag{39}$$

where the mass difference constant is defined as $\Gamma = \sum_i f_i (1 - M_i/\overline{M})^2 = c(1-c)/(12+c)^2$, and $S_0 = 2.62 \times 10^{-20}$ m^2 denotes the average area per carbon atom in graphene. As a result, the phonon relaxation time for resistive scattering is obtained based on Mathiessen's rule: $1/\tau_R(\omega,p,T) = 1/\tau_U(\omega,p,T) + 1/\tau_I(\omega,p)$ from Eq. (37) and Eq. (39).

A. Heat transport in an infinite graphene ribbon

First we consider heat transport in an infinite graphene ribbon to validate the adopted phonon properties including the dispersion relations and relaxation time expressions. The bulk thermal conductivity based on the phonon Boltzmann equation under Callaway's model is [30] $\kappa = \kappa_{SMRT} + \kappa_C$, with κ_{SMRT} and κ_C respectively the SMRT result and Callaway's correction term for normal scattering:

$$\kappa_{SMRT} = \frac{1}{2h_0} \sum_p \int \tau_C v_g^2 C_{\omega,p} d\omega, \tag{40}$$

$$\kappa_C = \frac{\left[\frac{1}{2h_0}\sum_p \int \frac{\tau_C}{\tau_N}\frac{k v_g}{\omega} C_{\omega,p} d\omega\right]^2}{\frac{1}{2h_0}\sum_p \int \frac{\tau_C}{\tau_N \tau_R}\frac{k^2}{\omega^2} C_{\omega,p} d\omega}, \tag{41}$$

where the combinational phonon relaxation time is defined as $1/\tau_C = 1/\tau_N + 1/\tau_R$, and the thickness of monolayer graphene $h_0 = 3.35 \times 10^{-10}$ m. As shown in Fig. 2, Callaway's model provides a prediction of the temperature-dependent thermal conductivity of an infinite graphene ribbon

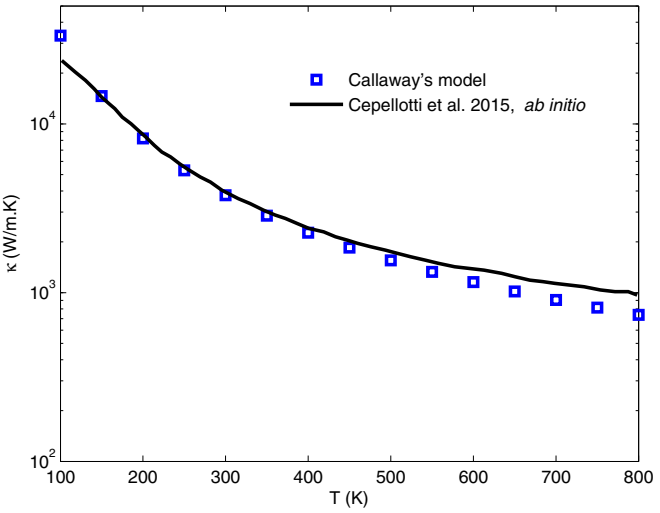

FIG. 2. Temperature-dependent thermal conductivity of an infinite suspended monolayer graphene ribbon: the solid line represents the *ab initio* solution of the linearized phonon Boltzmann equation with a full scattering term [25], whereas the squares denote the Callaway lattice thermal conductivity model with phonon properties adopted in the present work.

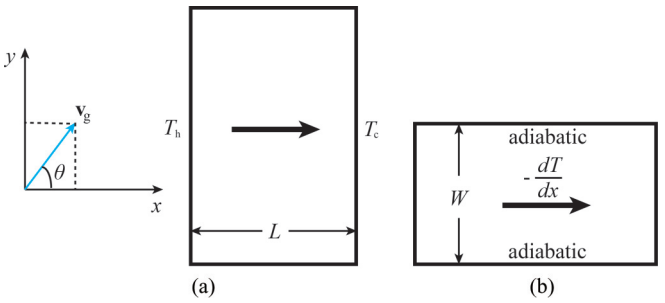

FIG. 3. Schematic of heat transport in (a) an infinitely wide graphene ribbon with a length L and (b) an infinitely long graphene ribbon with a width W.

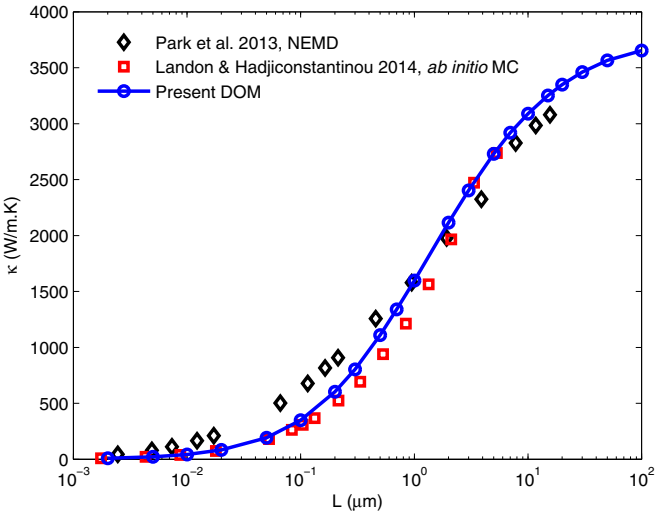

FIG. 4. Length-dependent effective thermal conductivity of an infinitely wide suspended monolayer graphene ribbon at room temperature ($T = 300$ K): the diamonds and squares represent the nonequilibrium molecular dynamics (NEMD) simulation results [56] and *ab initio* Monte Carlo (MC) solution of the linearized phonon Boltzmann equation with a full scattering term [20], respectively, whereas the line with circles denotes the present discrete-ordinate-method (DOM) solution of the phonon Boltzmann equation under Callaway's model with $N_x = 101$, $N_L = 8$, $N_T = 8$, $N_Z = 8$, $N_\theta = 32$.

in overall good agreement with the results from the *ab initio* solution of the phonon Boltzmann equation with the full scattering term [25]. Two points are thus inferred: (i) Callaway's model is a very good approximation to the full scattering term in the phonon Boltzmann equation for heat transport in graphene, consistent with the conclusion in a recent study [25]; (ii) the isotropic linear phonon dispersion relations and power-law relaxation time expressions represent an acceptable assumption for the present study. The suspended monolayer graphene ribbon is investigated throughout this work, with natural abundancy considered unless noted otherwise. The present numerical framework is also available for modeling heat transport in a bilayer or multilayer graphene ribbon [22,53] and a supported graphene ribbon [54,55] when the interlayer phonon scattering and phonon-substrate scattering rates are provided.

B. Heat transport in an infinitely wide graphene ribbon

In this subsection, the one-dimensional (1D) heat transport in an infinitely wide graphene ribbon shown in Fig. 3(a) is studied. The DOM scheme in Sec. II reduces to a 1D formulation with vanishing dependence on the y coordinate. Isothermal boundary conditions are implemented on the left-hand hot source and right-hand cold source. The same phonon transport process is modeled in a previous nonequilibrium molecular dynamics (NEMD) study [56], where a rectangular graphene ribbon was set between a hot thermostat and a cold thermostat. A periodic boundary condition was applied in the lateral direction such that the width of graphene ribbon was infinite [56]. For atomic interaction, the optimized Tersoff potential [57] was used, which has been shown to be the most suitable one in describing thermal properties of graphene [15]. The atomic mass of the carbon atom was also corrected accounting for the natural abundancy of ^{13}C [56]. Therefore a direct comparison between the present DOM solution and the NEMD result becomes possible, as shown in Fig. 4. The length-dependent effective thermal conductivity of an infinitely wide graphene ribbon at room temperature predicted by the present DOM solution agrees generally well with the NEMD data. The *ab initio* MC solution of the linearized phonon Boltzmann equation with the full scattering term for the same phonon heat transport case [20] is also included in Fig. 4 for comparison. The overall consistency between the DOM, NEMD, and *ab initio* MC results demonstrates the good performance of our numerical framework. A spatial grid $N_x = 101$, spectral nodes $N_L = N_T = N_Z = 8$, and angular resolution $N_\theta = 32$ have been used in the present numerical solution after an independence check.

Then a comparison is made between the present numerical results to experimental measurements on a graphene ribbon suspended over a circular hole with a diameter D by the Raman spectroscopy method [58,59]. The temperature decay after a laser heating of the graphene ribbon is detected via Raman signal to extract the effective thermal conductivity of the graphene ribbon through fitting the Fourier conduction model. A direct solution of the phonon Boltzmann equation for such a physical process is difficult. Instead, we make the length L of the graphene ribbon in our numerical simulation to match the diameter D of the hole as done in previous work [28]. In this way, we obtain the effective thermal conductivity of the graphene ribbon, which shows good agreement with the experimental data for different sizes of graphene ribbon in Fig. 5. The effective thermal conductivity decreases with increasing temperature due to the enhanced phonon umklapp scattering rate. On the other hand, the effective thermal conductivity is reduced at a smaller ribbon size because of more frequent phonon-boundary scattering. This indicates that the heat transport still deviates from the diffusive regime even in a graphene ribbon with micrometer size. Furthermore, the effect of isotope concentration on heat transport in a graphene ribbon is studied. As seen in Fig. 6, when the abundancy of ^{13}C increases from 1.1% to 50%, the effective thermal conductivity of the graphene ribbon reduces about 26% from 2355.5 (W/m K) to 1750.9 (W/m K) at room temperature. The reduction of the effective thermal conductivity comes from the

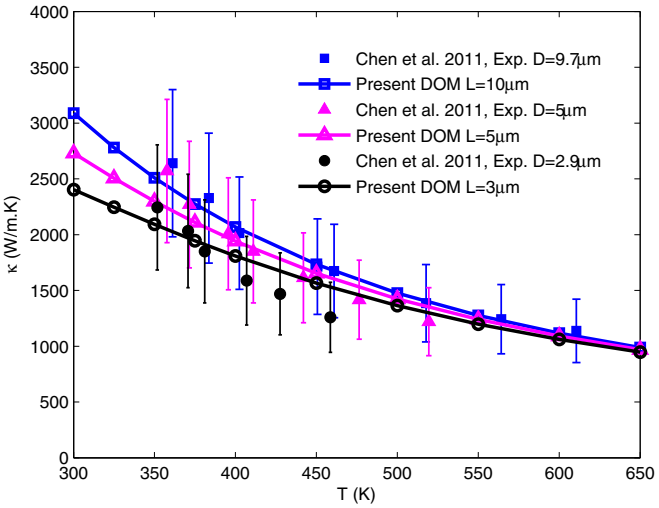

FIG. 5. Temperature-dependent effective thermal conductivity of a suspended monolayer graphene ribbon with different sizes: the filled squares, filled triangles, and filled circles with error bars represent the experimental results of a graphene ribbon with a diameter $D = 9.7\ \mu$m, 5 μm, and 2.9 μm, respectively [58], whereas the hollow-square line, hollow-triangle line, and hollow-circle line denote the present discrete-ordinate-method (DOM) solutions of the phonon Boltzmann equation under Callaway's model for an infinitely wide graphene ribbon with a length $L = 10\ \mu$m, 5 μm, and 3 μm, respectively, with $N_x = 101$, $N_L = 8$, $N_T = 8$, $N_Z = 8$, $N_\theta = 32$.

isotope scattering attributed to the mass difference between ^{12}C and ^{13}C. As a result, when the abundancy of ^{13}C further

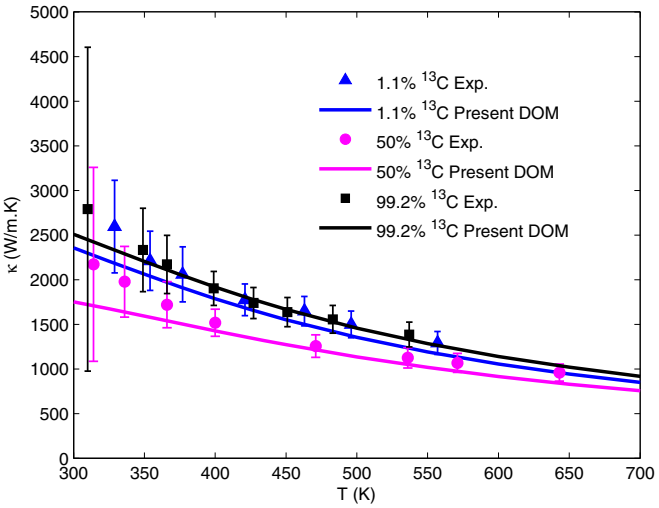

FIG. 6. Temperature-dependent effective thermal conductivity of a suspended monolayer graphene ribbon at different isotope concentrations: the filled triangles, filled circles, and filled squares with error bars represent the experimental results of a graphene ribbon with a diameter $D = 2.8\ \mu$m at 1.1%, 50%, and 99.2% ^{13}C concentrations, respectively [59], whereas the solid lines denote the present discrete-ordinate-method (DOM) solution of the phonon Boltzmann equation under Callaway's model for an infinitely widely graphene ribbon with a length $L = 2.8\ \mu$m at 1.1%, 50%, and 99.2% ^{13}C concentrations, respectively, with $N_x = 101$, $N_L = 8$, $N_T = 8$, $N_Z = 8$, $N_\theta = 32$.

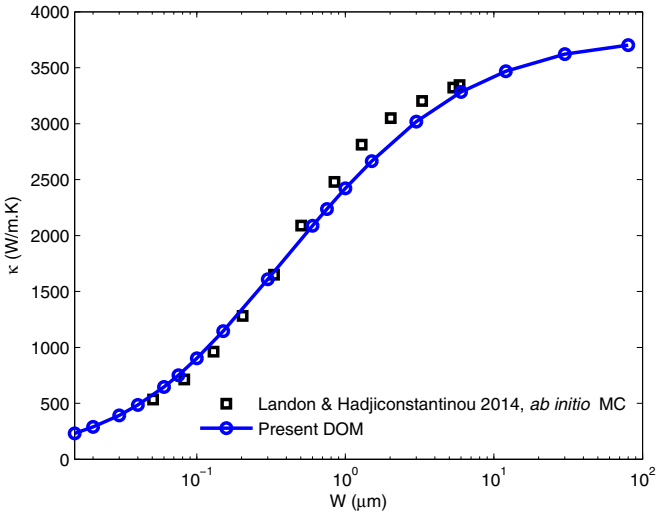

FIG. 7. Width-dependent effective thermal conductivity of an infinitely long suspended monolayer graphene ribbon at room temperature ($T = 300$ K): the squares represent the *ab initio* Monte Carlo (MC) solution of the linearized phonon Boltzmann equation with the full scattering term [20], whereas the line with circles denotes the present discrete-ordinate-method (DOM) solution of the phonon Boltzmann equation under Callaway's model with $N_x = 2$, $N_y = 101$, $N_L = 8$, $N_T = 8$, $N_Z = 8$, $N_\theta = 96$.

increases up to 99.2%, the effective thermal conductivity recovers nearly the same value as that of the graphene ribbon with natural abundancy. The overall good agreement between the present DOM solution and experimental results indicates that our numerical framework is capable of modeling heat transport in a graphene ribbon with isotope variation.

C. Heat transport in an infinitely long graphene ribbon

In this subsection, the two-dimensional heat transport in an infinitely long graphene ribbon shown in Fig. 3(b) is simulated by the present DOM scheme. The periodic heat flux boundary condition introduced in Sec. II C 3 is applied on both the left-hand and right-hand ends of the simulation domain to exert a constant temperature gradient along the heat transport direction with infinite dimension. For the adiabatic lateral edge of the graphene ribbon, the nonthermalizing diffuse scheme introduced in Sec. II C 2 is used. The present DOM solution produces the width-dependent effective thermal conductivity in good agreement with the *ab initio* MC solution of the linearized phonon Boltzmann equation with the full scattering term [20], as shown in Fig. 7. A spatial grid $N_x = 2$, $N_y = 101$, spectral nodes $N_L = 8, N_T = 8, N_Z = 8$, and angular resolution $N_\theta = 96$ have been adopted in the present numerical simulation after independence verification.

D. Heat transport in a rectangular graphene ribbon

In this subsection, we consider heat transport in a rectangular graphene ribbon with both a finite length and finite width as seen in Fig. 8. In contrast to the case in Sec. III C, isothermal boundary conditions are applied on the left-hand and right-hand ends of the simulation domain. The nonthermalizing diffuse scheme is still used for the adiabatic lateral edge. We

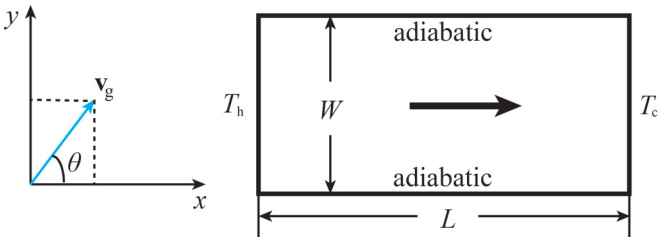

FIG. 8. Schematic of heat transport in a rectangular graphene ribbon with a length L and width W.

compare the effective thermal conductivity of graphene ribbon predicted by the present DOM solution to the results in a recent well-known experimental measurement on a graphene ribbon with a width 1.5 μm and a length from 300 nm to 9 μm [34]. A spatial grid $N_x = 101$, $N_y = 51$, spectral nodes $N_L = N_T = N_Z = 8$, and angular resolution $N_\theta = 48$ are used in the present numerical simulation after an independence check. The agreement between the DOM solution and experimental data is appreciably good when the length of the graphene ribbon is smaller than about 1 μm, as shown in Fig. 9. However, the experimental results are lower than the predicted effective thermal conductivity at larger length of the graphene ribbon. This overestimation has also been obtained in previous theoretical modeling of the same heat transport in a rectangular graphene ribbon [20,28,33]. It may be explained by the factors in a realistic situation such as finite graphene grain size and defects that have been neglected in the present modeling and that would induce further phonon scattering and thermal resistance. The *ab initio* MC solution of the linearized phonon Boltzmann equation with the full scattering term [20] is also

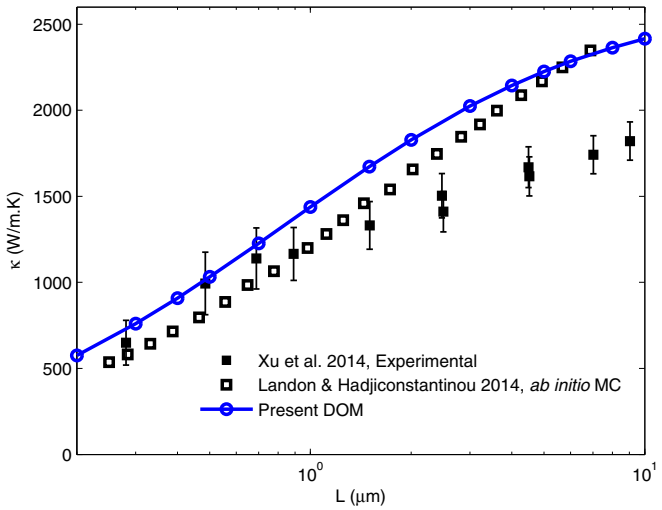

FIG. 9. Length-dependent effective thermal conductivity of suspended monolayer rectangular graphene ribbon with a width 1.5 μm at room temperature ($T = 300$ K): the filled squares with error bars represent the experimental data [34], the hollow squares represent the *ab initio* Monte Carlo (MC) solution of the linearized phonon Boltzmann equation with the full scattering term [20], whereas the line with circles denotes the present discrete-ordinate-method (DOM) solution of the phonon Boltzmann equation under Callaway's model with $N_x = 101$, $N_y = 51$, $N_L = 8$, $N_T = 8$, $N_Z = 8$, $N_\theta = 48$.

included for a comparison, which shows a general consistence with the present DOM solution. The slight difference between DOM and *ab initio* MC results may be attributed to the present simplification of the phonon dispersion and relaxation time. In all, the present DOM numerical framework displays an overall good performance in modeling heat transport through finite-size nano- and micro-graphene-ribbons.

IV. RESULTS AND DISCUSSION

In this section, we will apply the validated numerical methodology to study several important issues in heat transport through two-dimensional materials. As our method makes a direct treatment of the phonon-boundary scattering, we adopt it as a benchmark to evaluate the empirical expressions of the boundary scattering rate in previous *ab initio* solutions of the phonon Boltzmann equation or in Callaway's lattice thermal conductivity model in Sec. IV A. Furthermore, the present method is an efficient platform for modeling heat transport in a rectangular graphene ribbon with various lengths and widths. Thus we explore the width influence on the long debating length divergence of lattice thermal conductivity of graphene ribbon in Sec. IV B. Finally, we investigate the phonon Knudsen minimum and provide a theoretical prediction of it in the graphene ribbon system. The existence condition of this special hydrodynamic phenomenon is also quantified. Through the present methodology, it becomes feasible to obtain the details of spatial dependent heat flow profiles, which are crucial to understand the physical picture and underlying mechanism of heat transport through two-dimensional materials.

A. Examining the empirical boundary scattering rate

In the *ab initio* solution of the linearized phonon Boltzmann equation with the full scattering term, the phonon-boundary scattering is treated by adding an additional homogeneous scattering rate into the intrinsic scattering matrix [19,20,23,24,27]. Since phonon-boundary scattering at the interface is essentially different from the intrinsic phonon scattering within the material, such a treatment may introduce some error. As shown in a recent work [20], the maximal error by the widely used boundary scattering rate $1/\tau_B = 2|v_{gy}|/W$ reaches the order of 30% at room temperature. When such a boundary scattering rate is added to the resistive scattering rate in Eq. (40) and Eq. (41), i.e., $1/\tau_R = 1/\tau_U + 1/\tau_I + 1/\tau_B$, Callaway's lattice thermal conductivity model produces exactly the same result as the *ab initio* solution, as seen in Fig. 10(a). Actually, there are several different empirical expressions for the boundary scattering rate in the *ab initio* solution or Callaway's lattice thermal conductivity model, as summarized in Table I for heat transport in an infinitely long graphene ribbon. The empirical expressions for heat transport in an infinitely wide graphene ribbon are similar except a substitution of W and $|v_{gy}|$ by L and $|v_{gx}|$, respectively. These empirical expressions originate from the Fuchs-Sondheimer (F-S) model for phonon transport [55,60], with $1/\tau_B = 2|v_{gy}|/W$ being the small-width limit and $1/\tau_B = |v_{gy}|/W$ being the large-width limit. As the F-S model is based on the phonon Boltzmann equation under the SMRT approximation, it remains elusive whether it is plausible to incorporate the F-S boundary scattering

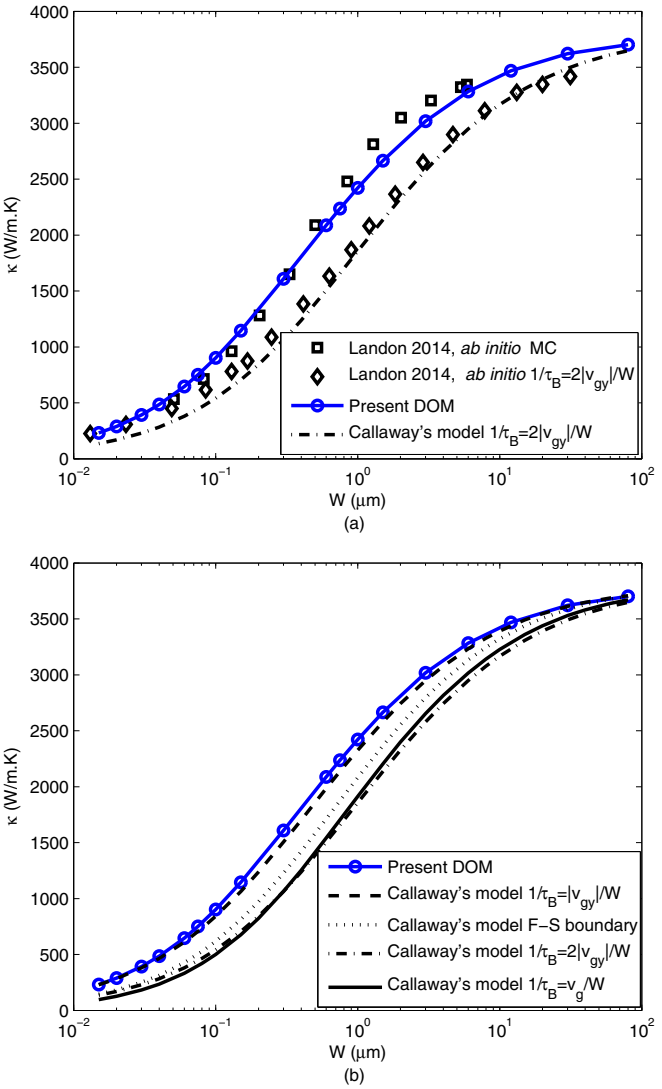

FIG. 10. Width-dependent effective thermal conductivity of an infinitely long suspended monolayer graphene ribbon at room temperature ($T = 300$ K): (a) comparison between the present DOM solution of the phonon Boltzmann equation under Callaway's model (line with circles) and the *ab initio* MC solution of the linearized phonon Boltzmann equation with the full scattering term (hollow squares) [20], and between Callaway's lattice thermal conductivity model (dot-dashed line) and the *ab initio* solution of the linearized phonon Boltzmann equation with the full scattering term (hollow diamonds) [20] with the same empirical expression of the boundary scattering rate; (b) comparison between the present DOM solution of the phonon Boltzmann equation under Callaway's model (line with circles) and Callaway's lattice thermal conductivity model with different empirical expressions of boundary scattering rates (cf. Table I).

rates into Callaway's lattice thermal conductivity model [33]. Therefore we examine Callaway's lattice thermal conductivity model with the empirical boundary scattering rates in Table I through comparing to the present DOM solution. As shown in Fig. 10(b), most of the empirical boundary models will result in an appreciable amount of underestimation as large as 30% at room temperature. It is also found that Callaway's lattice thermal conductivity model with boundary scattering rate $1/\tau_B = |v_{gy}|/W$ represents an acceptable approximation to the direct DOM solution.

We also examine Callaway's lattice thermal conductivity model with empirical boundary scattering rates for heat transport in a rectangular graphene ribbon, as summarized in Table II. The physical and numerical model is the same as that in Sec. III D, with the results given in Fig. 11. The simple boundary scattering rate $1/\tau_B = v_g(1/W + 1/L)$ overestimates the effective thermal conductivity of the graphene ribbon when its length L is smaller than the width $W = 1.5\mu$m, whereas it underestimates the value when its length is larger than the width. This can be explained by the fact that this boundary model averages the phonon scatterings from length edge and from width edge, and does not distinguish between them. Similar results and trends are obtained for Callaway's lattice thermal conductivity model with the other F-S empirical boundary scattering rate. A direct numerical solution of the phonon Boltzmann equation is indispensable for describing heat transport through a rectangular graphene ribbon. The current deterministic *ab initio* approaches are not capable of modeling such a heat transport case due to the limitation from the treatment of phonon-boundary scattering. The present methodology provides an efficient tool for fast evaluation of the effective thermal conductivity of a graphene ribbon with different geometrical shapes including rectangular, triangular, trapezoidal, and so on. The DOM scheme avoids the numerical fluctuations in *ab initio* MC scheme [20] especially in the near-continuum regime. In addition, the present method based on the phonon Boltzmann equation is applicable for a much broader range of graphene ribbon size in comparison to the MD simulation.

B. Length divergence of lattice thermal conductivity of graphene ribbon

The lattice thermal conductivity of three-dimensional dielectric materials is known to converge to a constant value as the system size increases unlimitedly. The situation becomes much more complicated for heat transport in low-dimensional nanomaterials. The lattice thermal conductivity of a one-dimensional momentum-conserving system has been theoretically predicted to diverge with the system size as $\kappa \propto L^{\alpha}$ with $\alpha \approx 1/3$ [61], and experimentally verified in carbon nanotubes up to millimeter-scale length [62]. For the two-dimensional system, the numerical study on nonlinear lattices [63] shows the thermal conductivity increases with lattice length logarithmically. In contrast, a macroscopic upper limit of thermal conductivity of graphene ribbon is obtained in direct molecular dynamics simulations [56,64]. In a recent experimental measurement [34], the lattice thermal conductivity of a graphene ribbon demonstrates a logarithmic dependence on the ribbon length from 300 nm to 9 μm. This logarithmic divergence has been later uncovered to be attributed to the hydrodynamic phonon transport driven by the nonresistive normal scattering for ribbon length smaller than 100 μm, while a convergence will be reached for ribbon length beyond 100 μm due to the coupling between in-plane and out-of-plane phonon modes [33]. A strong width dependence of lattice thermal conductivity for a specific

TABLE I. Summary of empirical expressions for the boundary scattering rate in the *ab initio* solution of the linearized phonon Boltzmann equation with the full scattering term or in Callaway's lattice thermal conductivity model for heat transport in an infinitely long graphene ribbon. τ_{int} is the relaxation time of intrinsic phonon scattering processes: $1/\tau_{int} = 1/\tau_U + 1/\tau_I + 1/\tau_N$.

Empirical expressions	Description	References
$\frac{1}{\tau_B} = \frac{\lvert v_{gy}\rvert}{W}\frac{1-\exp(-W/\tau_{int}\lvert v_{gy}\rvert)}{1-\tau_{int}\lvert v_{gy}\rvert/W[1-\exp(-W/\tau_{int}\lvert v_{gy}\rvert)]}$	Fuchs-Sondheimer (F-S) model	[33]
$\frac{1}{\tau_B} = \frac{\lvert v_{gy}\rvert}{W}$	Large width limit of F-S model	[24]
$\frac{1}{\tau_B} = \frac{2\lvert v_{gy}\rvert}{W}$	Small width limit of F-S model	[19–21,27]
$\frac{1}{\tau_B} = \frac{v_g}{W}$	Empirical	[23]

graphene ribbon length is found in recent theoretical studies [28,33,65]. However, the influence of the graphene ribbon width on the length divergence or convergence of lattice thermal conductivity remains ambiguous. Previous MD simulations [56,64] consider the infinitely wide graphene ribbon limited by computational capability, whereas the experimental study [34] uses a graphene ribbon with a specified width caused by the difficulty in sample preparation. As our computational method provides a feasible avenue to modeling heat transport in a rectangular graphene ribbon with arbitrary length and width, we explore such a width-dependent length divergence of the lattice thermal conductivity.

We consider the heat transport at room temperature in a rectangular graphene ribbon with a width 100 nm, 500 nm, and 1.5 μm, and various lengths from a few tens of nanometers to hundreds of micrometers. The physical and numerical model for the DOM solution is the same as that in Sec. III D. The length-dependent effective thermal conductivity of graphene ribbons at different widths is shown in Fig. 12. For the graphene ribbon with a width 1.5 μm consistent with that in a recent experimental study [34], a nearly logarithmic dependence of thermal conductivity is obtained for ribbon lengths within 0.1 μm $\sim$ 10 μm, which exactly covers the length scope 300 nm $\sim$ 9 μm of the measured samples in Ref. [34]. The lattice thermal conductivity converges to an upper limit beyond a length at about 80 μm. The convergence of lattice thermal conductivity will be reached at a smaller length of about 50 μm and 10 μm for a smaller ribbon width of 500 nm and 100 nm, respectively. On the other hand, the upper limit of the thermal conductivity will also reduce with decreasing ribbon width, with a value about 2600 (W/m K), 1900 (W/m K), and 900 (W/m K) for a width 1.5 μm, 500 nm, and 100 nm, respectively.

To understand the physical mechanism of width-dependent length convergence of lattice thermal conductivity, we further demonstrate the heat flow details in thermal transport through a graphene ribbon. The normalized cross-sectional heat flux profiles in a graphene ribbon with a width 100 nm and 1.5 μm at various lengths are given in Fig. 13(a) and Fig. 13(b), respectively. For a specific ribbon width, the heat flux profile will develop gradually with increasing ribbon length, and approaches the infinite-length limit finally. The heat flux profile at the infinite-length limit is very dependent on the ribbon width: a larger width results in a profile closer to the bulk limit. The results can be explained from the perspective of thermal resistance mainly as a function of the ratio of average phonon mean-free path (MFP) to ribbon size. The intrinsic average phonon MFP of monolayer graphene has been reported to be on the order of magnitude of 1 μm [11,56,66]. The effective MFP of phonon transport along a sufficiently long graphene ribbon will be affected by the lateral size, i.e., the ribbon width. When the ribbon width is smaller than the intrinsic average MFP, the MFP is reduced by the lateral boundary confinement to an effective value approximately the ribbon width. When the ribbon width is larger than the intrinsic average MFP, the effective MFP remains almost the intrinsic value. Therefore, for the considered graphene ribbons with a width 100 nm, 500 nm, and 1.5 μm, the effective MFPs are estimated as 100 nm, 500 nm, and 1 μm, respectively. To reach the infinite-length limit of heat transport, the ribbon length should be larger than about 100 times the effective phonon MFP, inversely the average Knudsen number smaller than 0.01 corresponding to the continuum limit. As a result, we acquire the width-dependent length convergence of lattice thermal conductivity of a graphene ribbon with the convergence length about 10 μm, 50 μm, and 100 μm separately. For a graphene ribbon with a width larger than 1.5 μm, the convergence length lies more or less within the range of one to a few hundred micrometers. The estimated convergence lengths based on the present MFP analysis are generally consistent with the results obtained in Fig. 12.

C. Phonon Knudsen minimum and existence condition

The Knudsen minimum phenomenon was first observed by Knudsen in 1909 in his experimental study of rarefied gas flow through glass capillary tubes in transition and free molecular flow regimes [67]. The mass flow rate normalized

TABLE II. Summary of empirical expressions for the boundary scattering rate in Callaway's lattice thermal conductivity model for heat transport in a rectangular graphene ribbon.

Empirical expressions	Description	References
$\frac{1}{\tau_B} = \frac{v_g}{L_E}$	Empirical: $1/L_E = 1/W + 1/L$	[32]
$\frac{1}{\tau_B} = \frac{1}{\tau_{B,L}} + \frac{1}{\tau_{B,W}}$	Both $\frac{1}{\tau_{B,L}}$ and $\frac{1}{\tau_{B,W}}$ using the Fuchs-Sondheimer (F-S) model	[33]

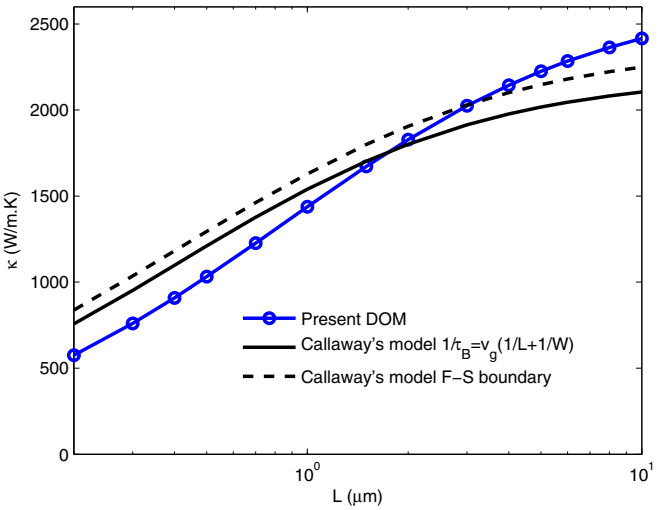

FIG. 11. Length-dependent effective thermal conductivity of a suspended monolayer rectangular graphene ribbon with a width 1.5 μm at room temperature ($T = 300$ K): the line with circles denotes the present discrete-ordinate-method (DOM) solution of the phonon Boltzmann equation under Callaway's model, whereas the solid line and dashed line represent Callaway's lattice thermal conductivity model with empirical expressions of the boundary scattering rate (cf. Table II).

by its free molecular flow limit shows a minimum at Kn $\sim$ 1. This interesting phenomenon provides important information about the scaling of transport resistance in different gas flow regimes, and has induced lots of theoretical and experimental studies [67]. A similar effect in phonon transport has also

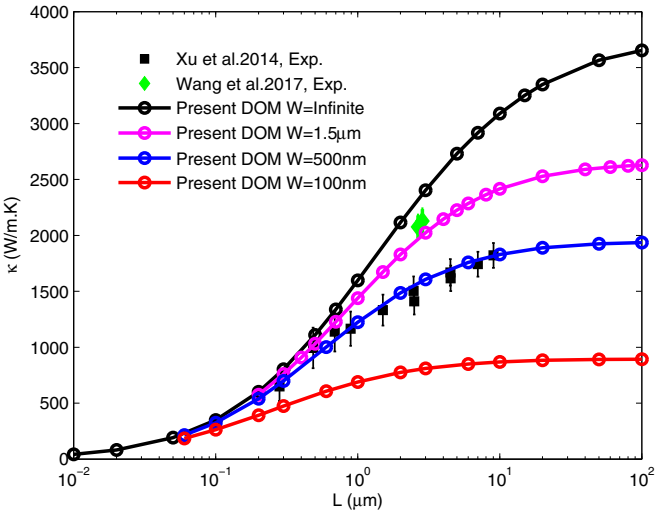

FIG. 12. Length-dependent effective thermal conductivity of a suspended monolayer rectangular graphene ribbon with different widths at room temperature ($T = 300$ K): the filled squares denote the experimental data at 300 K of a graphene ribbon with a width 1.5 μm from the literature [34], the filled diamonds denote the experimental data at 297 K of graphene ribbon sample 1 with a width 2.8 μm and sample 4 with a width 4.08 μm from the literature [35], whereas the solid lines with circles denote the present results by the DOM solution of the phonon Boltzmann equation under Callaway's model.

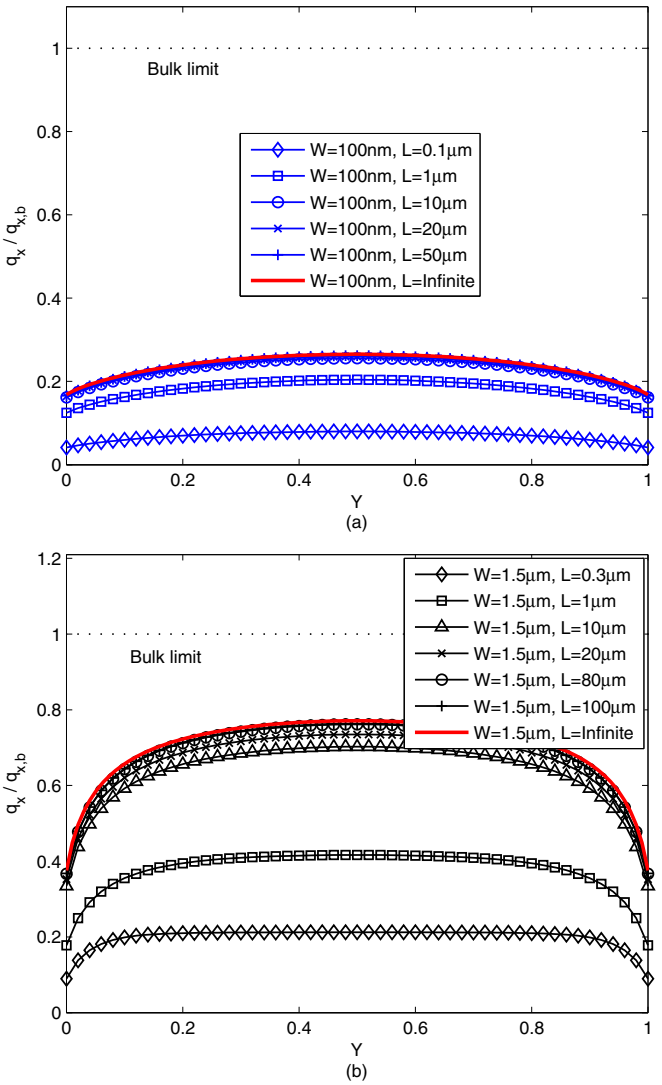

FIG. 13. Normalized cross-sectional heat flux distributions along the vertical center line in heat transport through a suspended monolayer rectangular graphene ribbon at room temperature ($T = 300$ K): (a) graphene width 100 nm; (b) graphene width 1.5 μm. The red solid lines denote the infinite-length limit (cf. Sec. III C), whereas the dashed lines denote the bulk limit (infinite graphene).

been obtained in theoretical calculation [68] and observed in experimental measurement [69,70] in liquid helium below 0.7 K. Although the phonon Knudsen minimum has been anticipated to exist in a dielectric solid or semiconductor when the normal process is dominant and size effect plays a role [1,26], it has not yet been directly predicted or observed in solids due to the lacking of feasible computational or experimental methodology, to our best knowledge. Since the heat transport in a graphene ribbon satisfies the mentioned prerequisites, we provide a theoretical prediction of the phonon Knudsen minimum in a solid based on the DOM solution of the phonon Boltzmann equation under Callaway's model. The physical and numerical models here are the same as those in Sec. III C.

To separate the effect of phonon scattering from carbon isotopes, we first consider heat transport in an isotopically

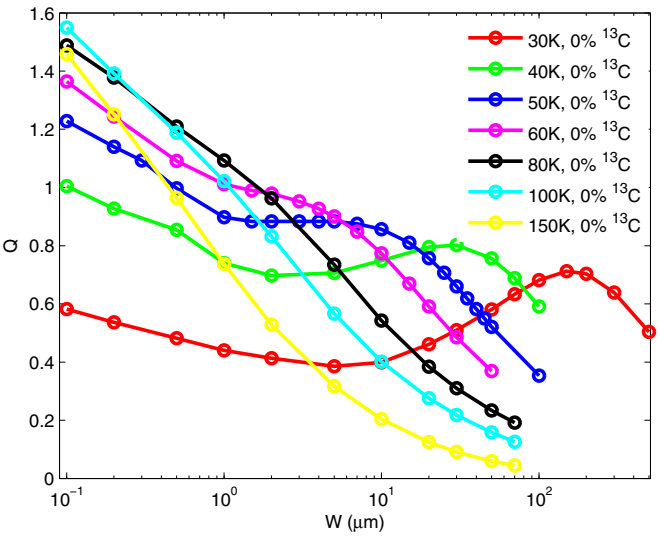

FIG. 14. Nondimensional heat flow rate versus width of an infinitely long suspended monolayer graphene ribbon with 0% ^{13}C (isotopically pure) at different temperatures: Knudsen's minimum is obtained at temperature smaller than about 50 K.

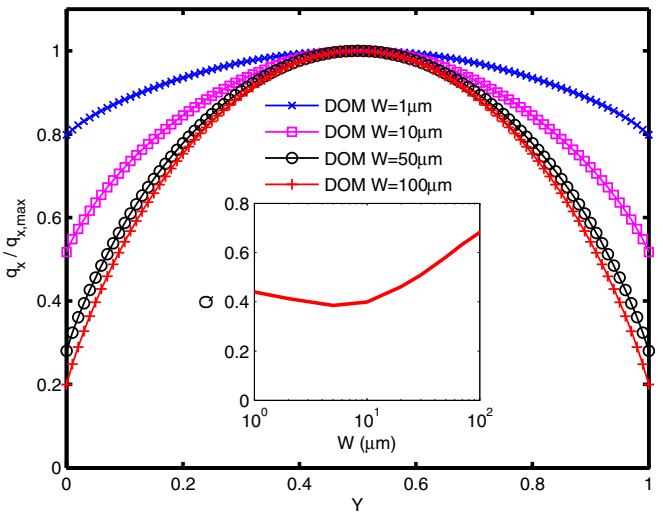

FIG. 15. Evidence of phonon Poiseuille flow and Knudsen's minimum: normalized cross-sectional heat flux distribution in heat transport through an infinitely long suspended monolayer graphene ribbon with 0% ^{13}C (isotopically pure) at 30 K. The inset figure demonstrates the phonon Knudsen minimum which take places at about a graphene width of 10 μm.

pure graphene ribbon. Similarly to the normalized mass flow rate in gas flow [67], the nondimensional heat flow rate is defined as the ratio of average heat flux to ballistic heat flux:

$$Q = \frac{\frac{1}{W}\int_0^W q_x(y)dy}{-\lambda_b \frac{W}{\langle\Lambda\rangle}\frac{dT}{dx}}, \tag{42}$$

which can be also understood as the effective thermal conductivity normalized by the Casimir limit: $\lambda_b \frac{W}{\langle\Lambda\rangle} \sim C_V \langle v_g \rangle W$ [68]. The average phonon mean-free path is calculated from $\langle\Lambda\rangle = \sum_p \int C_{\omega,p}\Lambda_{\omega,p}d\omega / \sum_p \int C_{\omega,p}d\omega$. The phonon Knudsen minimum is obtained when the temperature is smaller than about 50 K as shown in Fig. 14. Taking the typical numerical result at 30 K for analysis, the nondimensional heat flow rate decreases with increasing width and reaches a minimum at a width of about 10 μm (referred to as the first stage). Then the nondimensional heat flow rate starts to increase with increasing width and reaches a maximum at a width of about 100 μm (referred to as the second stage). Finally, the nondimensional heat flow rate decreases with increasing width again (referred to as the third stage). These three stages with distinct features are dictated by different heat transport mechanisms. In the first stage, heat transport is mainly dominated by phonon-boundary scattering, which is very similar to the microscale gas flow in the late transition regime and free molecular flow regime. The heat flux profile becomes more flattened as the graphene width decreases below 10 μm, which indicates a smaller thermal resistance and a larger nondimensional heat flow rate. In the second stage, the momentum-conserving phonon-phonon normal scattering becomes dominant over the phonon-boundary scattering. Phonon transport resembles the Poiseuille gas flow in the slip regime and early transition regime as shown in Fig. 15, where parabolic heat flux profiles with a slip at the boundary are observed. With the graphene width increasing from 10 to 100 μm, the rarefication effect and amount of heat flux slip decrease, and the total heat flow rate thus increases nearly as the well-known third power of width in the Poiseuille flow. As a transition from the first stage to the second stage, the phonon Knudsen minimum represents a balance between the rarefication effect due to boundary scattering and the collective effect due to normal scattering. In the third stage, some phonon umklapp scattering would take place as the width increases to be comparable to its mean-free path, where the heat flow rate is nearly proportional to the first power of the width. The obtained maximum denotes a balance between the normal scattering and umklapp scattering. When the average temperature in the graphene ribbon is higher (>50 K), the phonon normal scattering and its effect will be weakened in the second stage. The momentum-destroying phonon-phonon umklapp scattering will destroy the phonon Poiseuille flow and the heat flux profile becomes no longer parabolic, as shown in Fig. 16. The umklapp scattering tends to introduce homogeneous thermal transport resistance throughout the system such that the heat flux profile away from the boundary becomes nearly uniform. The phonon Knudsen minimum will disappear with the nondimensional heat flow rate continuously decreasing as the width is enlarging.

The effect of carbon isotopes on the phonon Knudsen minimum is then studied in a graphene ribbon at an average temperature 40 K, with the isotope concentration from isotopically pure (0% ^{13}C) to 5% ^{13}C taken into account. The phonon Knudsen minimum disappears when the concentration of ^{13}C is larger than about 0.5%, as shown in Fig. 17. The resistive phonon-isotope scattering has similar influence to that of phonon umklapp scattering on heat transport, and will destroy the collective effect from phonon normal scattering. With isotope concentration increasing from 0% to 5%, the heat flux profile turns from parabolic to exponential, as shown in Fig. 18. The hydrodynamic phonon transport in a graphene ribbon is very sensitive to the carbon isotope, a tiny amount

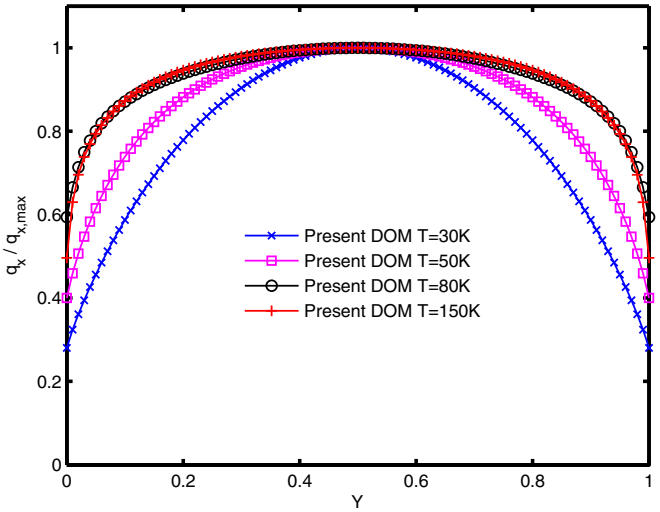

FIG. 16. Normalized cross-sectional heat flux distributions in heat transport through an infinitely long suspended monolayer graphene ribbon with 0% ^{13}C (isotopically pure) and a width 50 μm at different temperatures.

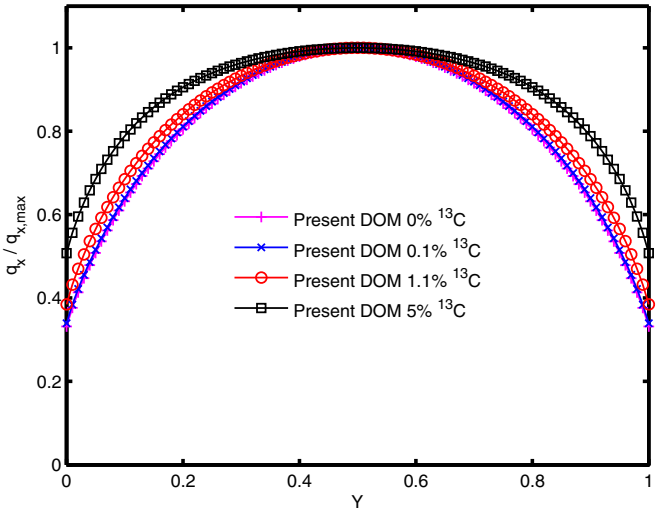

FIG. 18. Normalized cross-sectional heat flux distributions in heat transport through an infinitely long suspended monolayer graphene ribbon with a width 30 μm and different isotope concentrations at 40 K.

of which will deteriorate the hydrodynamic effects. In order to detect the experimental evidence of the phonon hydrodynamic phenomenon in two-dimensional nanomaterials predicted by recent theoretical studies [25,26], one should carefully control the isotope concentration in graphene ribbon. According to the present results, it is difficult to observe the hydrodynamic phonon transport in graphene ribbon with natural abundancy. The isotopically purified graphene ribbon [59] is recommended as a better platform for future experimental exploration.

To quantify the destruction effect of resistive phonon scattering including the umklapp scattering and isotope scattering, we compute the ratio of the average linewidth of normal scattering to that of intrinsic resistive scattering. The average linewidth of a specific phonon scattering has been defined as [25]

$$\Gamma_i = \left\langle \frac{2\pi}{\tau_i} \right\rangle = \frac{\sum_{\mathrm{p}} \int C_{\omega,\mathrm{p}} 2\pi/\tau_i(\omega,p,T) d\omega}{\sum_{\mathrm{p}} \int C_{\omega,\mathrm{p}} d\omega}, \quad (i = N,U,R). \tag{43}$$

The ratio of the average linewidth of normal scattering to that of intrinsic resistive scattering (Γ_N/Γ_R) versus temperature at different isotope concentrations in infinite graphene ribbon is given in Fig. 19. We deduce that the phonon Knudsen minimum can take place in a graphene ribbon only when

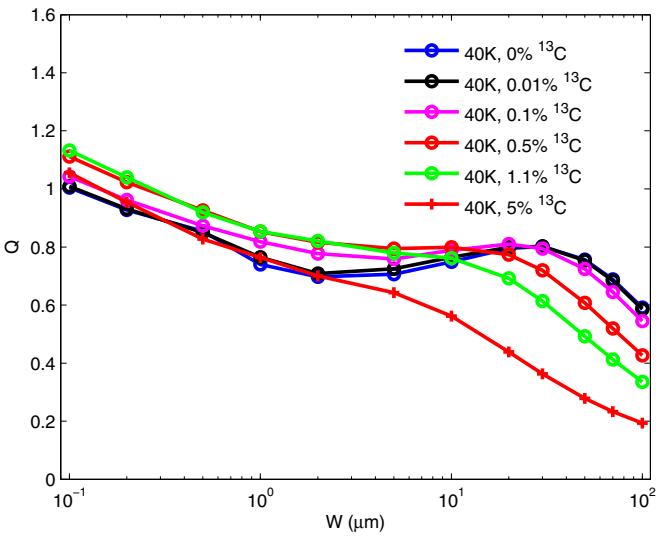

FIG. 17. Nondimensional heat flow rate versus width of an infinitely long suspended monolayer graphene ribbon with different isotope concentrations at 40 K. Knudsen's minimum is obtained at an isotope concentration smaller than about 0.5%.

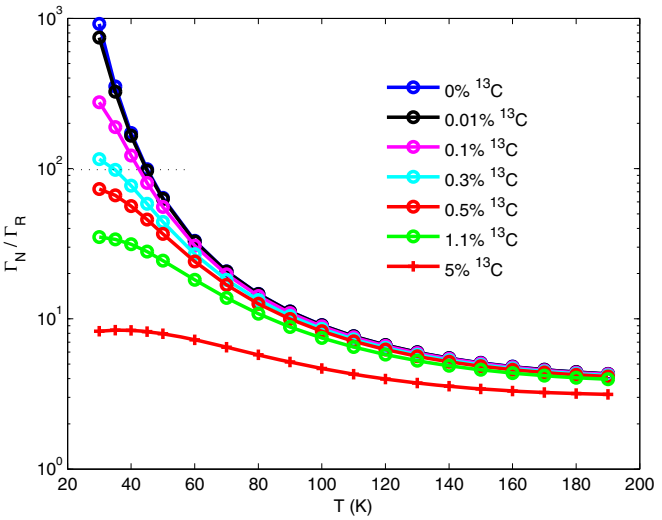

FIG. 19. Ratio of the average phonon normal scattering linewidth to the average intrinsic phonon resistive scattering linewidth versus temperature in an infinite suspended monolayer graphene ribbon at different isotope concentrations. The horizontal dashed line represents the threshold for existence of the phonon Knudsen minimum.

$\Gamma_N/\Gamma_R \geqslant 100$, i.e., when the average normal scattering rate is stronger than 100 times the average intrinsic resistive scattering rate. For an isotopically pure graphene ribbon, this condition is satisfied when the average temperature is lower than about 45 K, which is consistent with the threshold value (∼50 K) obtained in Fig. 14. At an average temperature 40 K, this condition is satisfied only when the abundancy of ^{13}C is smaller than about 0.3%, which is in accordance with the threshold value (∼0.5%) obtained in Fig. 17. Although normal scattering has been found to dominate over resistive scattering in graphene in the whole temperature scope [24–26], the phonon Knudsen's minimum could only be observed at very low temperature and low isotope concentration where the normal scattering rate is two orders of magnitude stronger than the intrinsic resistive scattering rate. Even a very small portion of resistive scattering would destroy the collective effect of normal scattering and this special hydrodynamic phenomenon.

V. CONCLUSIONS

We develop a discrete-ordinate-method (DOM) scheme for numerical solution of the phonon Boltzmann equation under Callaway's dual relaxation model to study heat transport in two-dimensional materials. Our scheme represents not only a good approximation to the *ab initio* calculation of phonon dynamics; it also overcomes the empirical treatment of phonon-boundary scattering in the latter. A validation of our methodology is demonstrated by modeling heat transport in infinitely wide, infinitely long, and rectangular graphene ribbons, which shows an overall good agreement with previous molecular dynamics simulation, *ab initio* Monte Carlo simulation, and experimental results. Callaway's lattice thermal conductivity model with several empirical boundary scattering expressions is evaluated and shown to overestimate or underestimate the DOM results. The length convergence of lattice thermal conductivity of rectangular graphene ribbon is found to be much dependent on the ribbon width. The convergence length is estimated to be about hundred times the effective phonon mean-free path (MFP) assumed as the smaller one among the ribbon width and the intrinsic average phonon MFP. The phonon Knudsen minimum is predicted to take place in a graphene ribbon only when the average normal scattering rate is stronger than 100 times the intrinsic resistive one at sufficiently low temperature and isotope concentration. The present methodology is also available for modeling heat transport in other promising two-dimensional nanomaterials such as the molybdenum disulphide, boron nitride, and so on [25]. It is straightforward as well to generalize our approach to one-dimensional [71] and three-dimensional [72] materials where the phonon collective effect is significant with potential new physics and more applications to be discovered in the future.

ACKNOWLEDGMENTS

The authors appreciate helpful discussions with X. P. Luo and M. Park. This work is financially supported by NSF of China Grants No. 51621062 and No. 51676107.

[1] G. Chen, *Nanoscale Energy Transport and Conversion: A Parallel Treatment of Electrons, Molecules, Phonons, and Photons* (Oxford University Press, New York, 2005).

[2] D. G. Cahill, P. V. Braun, G. Chen, D. R. Clarke, S. Fan, K. E. Goodson, P. Keblinski, W. P. King, G. D. Mahan, A. Majumdar, H. J. Maris, S. R. Phillpot, E. Pop, and L. Shi, Nanoscale thermal transport. II. 2003–2012, Appl. Phys. Rev. **1**, 011305 (2014).

[3] Y. Y. Guo and M. R. Wang, Phonon hydrodynamics and its applications in nanoscale heat transport, Phys. Rep. **595**, 1 (2015).

[4] M. Kaviany, *Heat Transfer Physics* (Cambridge University Press, New York, 2008).

[5] L. Shi, C. Dames, J. R. Lukes, P. Reddy, J. Duda, D. G. Cahill, J. Lee, A. Marconnet, K. E. Goodson, and J.-H. Bahk, Evaluating broader impacts of nanoscale thermal transport research, Nanoscale Microscale Thermophys. Eng. **19**, 127 (2015).

[6] A. L. Moore and L. Shi, Emerging challenges and materials for thermal management of electronics, Mater. Today **17**(4), 163 (2014).

[7] J. Cho, Z. Li, M. Asheghi, and K. E. Goodson, Near-junction thermal management: Thermal conduction in gallium nitride composite substrates, Annu. Rev. Heat Transfer **18**, 7 (2015).

[8] Z. Yan, G. Liu, J. Khan, and A. Balandin, Graphene quilts for thermal management of high-power GaN transistors, Nat. Commun. **3**, 827 (2012).

[9] H. Han, Y. Zhang, N. Wang, M. K. Samani, Y. Ni, Z. Y. Mijbil, M. Edwards, S. Xiong, K. Sääskilahti, and M. Murugesan, Functionalization mediates heat transport in graphene nanoflakes, Nat. Commun. **7**, 11281 (2016).

[10] A. A. Balandin, S. Ghosh, W. Bao, I. Calizo, D. Teweldebrhan, F. Miao, and C. N. Lau, Superior thermal conductivity of single-layer graphene, Nano Lett. **8**, 902 (2008).

[11] E. Pop, V. Varshney, and A. K. Roy, Thermal properties of graphene: Fundamentals and applications, MRS Bull. **37**, 1273 (2012).

[12] K. Khanafer and K. Vafai, A critical synthesis of graphene thermal properties and its applications, Adv. Heat Transfer **48**, 95 (2016).

[13] D. L. Nika and A. A. Balandin, Phonons and thermal transport in graphene and graphene-based materials, Rep. Prog. Phys. **80**, 036502 (2017).

[14] A. J. H. McGaughey and M. Kaviany, Phonon transport in molecular dynamics simulations: Formulation and thermal conductivity prediction, Adv. Heat Transfer **39**, 169 (2006).

[15] J.-H. Zou, Z.-Q. Ye, and B.-Y. Cao, Phonon thermal properties of graphene from molecular dynamics using different potentials, J. Chem. Phys. **145**, 134705 (2016).

[16] D. Nika, E. Pokatilov, A. Askerov, and A. Balandin, Phonon thermal conduction in graphene: Role of Umklapp and edge roughness scattering, Phys. Rev. B **79**, 155413 (2009).

[17] Z. Aksamija and I. Knezevic, Lattice thermal conductivity of graphene nanoribbons: Anisotropy and edge roughness scattering, Appl. Phys. Lett. **98**, 141919 (2011).

[18] M. Omini and A. Sparavigna, An iterative approach to the phonon Boltzmann equation in the theory of thermal conductivity, Phys. B (Amsterdam, Neth.) **212**, 101 (1995).
[19] G. Fugallo, M. Lazzeri, L. Paulatto, and F. Mauri, *Ab initio* variational approach for evaluating lattice thermal conductivity, Phys. Rev. B **88**, 045430 (2013).
[20] C. D. Landon and N. G. Hadjiconstantinou, Deviational simulation of phonon transport in graphene ribbons with *ab initio* scattering, J. Appl. Phys. **116**, 163502 (2014).
[21] L. Lindsay, D. Broido, and N. Mingo, Flexural phonons and thermal transport in graphene, Phys. Rev. B **82**, 115427 (2010).
[22] L. Lindsay, D. Broido, and N. Mingo, Flexural phonons and thermal transport in multilayer graphene and graphite, Phys. Rev. B **83**, 235428 (2011).
[23] L. Lindsay, W. Li, J. Carrete, N. Mingo, D. Broido, and T. Reinecke, Phonon thermal transport in strained and unstrained graphene from first principles, Phys. Rev. B **89**, 155426 (2014).
[24] G. Fugallo, A. Cepellotti, L. Paulatto, M. Lazzeri, N. Marzari, and F. Mauri, Thermal conductivity of graphene and graphite: Collective excitations and mean free paths, Nano Lett. **14**, 6109 (2014).
[25] A. Cepellotti, G. Fugallo, L. Paulatto, M. Lazzeri, F. Mauri, and N. Marzari, Phonon hydrodynamics in two-dimensional materials, Nat. Commun. **6**, 6400 (2015).
[26] S. Lee, D. Broido, K. Esfarjani, and G. Chen, Hydrodynamic phonon transport in suspended graphene, Nat. Commun. **6**, 6290 (2015).
[27] X. Gu and R. Yang, First-principles prediction of phononic thermal conductivity of silicene: A comparison with graphene, J. Appl. Phys. **117**, 025102 (2015).
[28] S. Mei, L. Maurer, Z. Aksamija, and I. Knezevic, Full-dispersion Monte Carlo simulation of phonon transport in micron-sized graphene nanoribbons, J. Appl. Phys. **116**, 164307 (2014).
[29] Y. Shen, G. Xie, X. Wei, K. Zhang, M. Tang, J. Zhong, G. Zhang, and Y.-W. Zhang, Size and boundary scattering controlled contribution of spectral phonons to the thermal conductivity in graphene ribbons, J. Appl. Phys. **115**, 063507 (2014).
[30] J. Callaway, Model for lattice thermal conductivity at low temperatures, Phys. Rev. **113**, 1046 (1959).
[31] J. Ma, W. Li, and X. Luo, Examining the Callaway model for lattice thermal conductivity, Phys. Rev. B **90**, 035203 (2014).
[32] A. Nissimagoudar and N. Sankeshwar, Significant reduction of lattice thermal conductivity due to phonon confinement in graphene nanoribbons, Phys. Rev. B **89**, 235422 (2014).
[33] A. K. Majee and Z. Aksamija, Length divergence of the lattice thermal conductivity in suspended graphene nanoribbons, Phys. Rev. B **93**, 235423 (2016).
[34] X. Xu, L. F. Pereira, Y. Wang, J. Wu, K. Zhang, X. Zhao, S. Bae, C. T. Bui, R. Xie, and J. T. Thong, Length-dependent thermal conductivity in suspended single-layer graphene, Nat. Commun. **5**, 3689 (2014).
[35] H. Wang, S. Hu, K. Takahashi, X. Zhang, H. Takamatsu, and J. Chen, Experimental study of thermal rectification in suspended monolayer graphene, Nat. Commun. **8**, 15843 (2017).
[36] S. Mazumder and A. Majumdar, Monte Carlo study of phonon transport in solid thin films including dispersion and polarization, J. Heat Transfer **123**, 749 (2001).
[37] J.-P. M. Peraud and N. G. Hadjiconstantinou, Efficient simulation of multidimensional phonon transport using energy-based variance-reduced Monte Carlo formulations, Phys. Rev. B **84**, 205331 (2011).
[38] A. Nabovati, D. P. Sellan, and C. H. Amon, On the lattice Boltzmann method for phonon transport, J. Comput. Phys. **230**, 5864 (2011).
[39] Y. Y. Guo and M. R. Wang, Lattice Boltzmann modeling of phonon transport, J. Comput. Phys. **315**, 1 (2016).
[40] R. G. Yang, G. Chen, M. Laroche, and Y. Taur, Simulation of nanoscale multidimensional transient heat conduction problems using ballistic-diffusive equations and phonon Boltzmann equation, J. Heat Transfer **127**, 298 (2005).
[41] A. J. Minnich, G. Chen, S. Mansoor, and B. Yilbas, Quasiballistic heat transfer studied using the frequency-dependent Boltzmann transport equation, Phys. Rev. B **84**, 235207 (2011).
[42] S. V. Narumanchi, J. Y. Murthy, and C. H. Amon, Simulation of unsteady small heat source effects in sub-micron heat conduction, J. Heat Transfer **125**, 896 (2003).
[43] S. V. Narumanchi, J. Y. Murthy, and C. H. Amon, Submicron heat transport model in silicon accounting for phonon dispersion and polarization, J. Heat Transfer **126**, 946 (2004).
[44] Z. L. Guo and K. Xu, Discrete unified gas kinetic scheme for multiscale heat transfer based on the phonon Boltzmann transport equation, Int. J. Heat Mass Transfer **102**, 944 (2016).
[45] X.-P. Luo and H.-L. Yi, A discrete unified gas kinetic scheme for phonon Boltzmann transport equation accounting for phonon dispersion and polarization, Int. J. Heat Mass Transfer **114**, 970 (2017).
[46] Z. Banach and W. Larecki, Chapman-Enskog method for a phonon gas with finite heat flux, J. Phys. A: Math. Theor. **41**, 375502 (2008).
[47] A. Majumdar, Microscale heat conduction in dielectric thin films, J. Heat Transfer **115**, 7 (1993).
[48] A. Cepellotti and N. Marzari, Transport waves as crystal excitations, Phys. Rev. Mater. **1**, 045406 (2017).
[49] B. S. Yilbas and S. B. Mansoor, Phonon transport and equivalent equilibrium temperature in thin silicon films, J. Non-Equilib. Thermodyn. **38**, 153 (2013).
[50] R. Yang and G. Chen, Thermal conductivity modeling of periodic two-dimensional nanocomposites, Phys. Rev. B **69**, 195316 (2004).
[51] Q. Hao, G. Chen, and M.-S. Jeng, Frequency-dependent Monte Carlo simulations of phonon transport in two-dimensional porous silicon with aligned pores, J. Appl. Phys. **106**, 114321 (2009).
[52] D. Morelli, J. Heremans, and G. Slack, Estimation of the isotope effect on the lattice thermal conductivity of group IV and group III-V semiconductors, Phys. Rev. B **66**, 195304 (2002).
[53] S. Ghosh, W. Bao, D. L. Nika, S. Subrina, E. P. Pokatilov, C. N. Lau, and A. A. Balandin, Dimensional crossover of thermal transport in few-layer graphene materials, Nat. Mater. **9**, 555 (2010).
[54] J. H. Seol, I. Jo, A. L. Moore, L. Lindsay, Z. H. Aitken, M. T. Pettes, X. Li, Z. Yao, R. Huang, D. Broido, N. Mingo, R. S. Ruoff, and L. Shi, Two-dimensional phonon transport in supported graphene, Science **328**, 213 (2010).
[55] Z. Aksamija and I. Knezevic, Thermal transport in graphene nanoribbons supported on SiO_2, Phys. Rev. B **86**, 165426 (2012).

[56] M. Park, S.-C. Lee, and Y.-S. Kim, Length-dependent lattice thermal conductivity of graphene and its macroscopic limit, J. Appl. Phys. **114**, 053506 (2013).

[57] L. Lindsay and D. Broido, Optimized Tersoff and Brenner empirical potential parameters for lattice dynamics and phonon thermal transport in carbon nanotubes and graphene, Phys. Rev. B **81**, 205441 (2010).

[58] S. Chen, A. L. Moore, W. Cai, J. W. Suk, J. An, C. Mishra, C. Amos, C. W. Magnuson, J. Kang, and L. Shi, Raman measurements of thermal transport in suspended monolayer graphene of variable sizes in vacuum and gaseous environments, ACS Nano **5**, 321 (2011).

[59] S. Chen, Q. Wu, C. Mishra, J. Kang, H. Zhang, K. Cho, W. Cai, A. A. Balandin, and R. S. Ruoff, Thermal conductivity of isotopically modified graphene, Nat. Mater. **11**, 203 (2012).

[60] J. E. Turney, A. J. H. McGaughey, and C. H. Amon, In-plane phonon transport in thin films, J. Appl. Phys. **107**, 024317 (2010).

[61] A. Dhar, Heat transport in low-dimensional systems, Adv. Phys. **57**, 457 (2008).

[62] V. Lee, C.-H. Wu, Z.-X. Lou, W.-L. Lee, and C.-W. Chang, Divergent and Ultrahigh Thermal Conductivity in Millimeter-Long Nanotubes, Phys. Rev. Lett. **118**, 135901 (2017).

[63] L. Wang, B. Hu, and B. Li, Logarithmic divergent thermal conductivity in two-dimensional nonlinear lattices, Phys. Rev. E **86**, 040101 (2012).

[64] G. Barbarino, C. Melis, and L. Colombo, Intrinsic thermal conductivity in monolayer graphene is ultimately upper limited: A direct estimation by atomistic simulations, Phys. Rev. B **91**, 035416 (2015).

[65] Y. Sonvane, S. K. Gupta, P. Raval, I. Lukačević, and P. B. Thakor, Length, width, and roughness dependent thermal conductivity of graphene nanoribbons, Chem. Phys. Lett. **634**, 16 (2015).

[66] S. Ghosh, I. Calizo, D. Teweldebrhan, E. P. Pokatilov, D. L. Nika, A. A. Balandin, W. Bao, F. Miao, and C. N. Lau, Extremely high thermal conductivity of graphene: Prospects for thermal management applications in nanoelectronic circuits, Appl. Phys. Lett. **92**, 151911 (2008).

[67] G. Karniadakis, A. Beskok, and N. Aluru, *Microflows and Nanoflows: Fundamentals and Simulation* (Springer, New York, 2005).

[68] D. Benin and H. J. Maris, Phonon heat transport and Knudsen's minimum in liquid helium at low temperatures, Phys. Rev. B **18**, 3112 (1978).

[69] R. W. Whitworth, Experiments on the flow of heat in liquid helium below 0.7 °K, Proc. R. Soc. London A **246**, 390 (1958).

[70] D. S. Greywall, Thermal-conductivity measurements in liquid ^{4}He below 0.7 K, Phys. Rev. B **23**, 2152 (1981).

[71] S. Lee and L. Lindsay, Hydrodynamic phonon drift and second sound in a (20, 20) single-wall carbon nanotube, Phys. Rev. B **95**, 184304 (2017).

[72] J. Al-Otaibi and G. P. Srivastava, Three-phonon scattering processes and thermal conductivity in IV-chalocogenides, J. Phys.: Condens. Matter **27**, 335801 (2015).